# Data-driven Bayesian inference for stochastic model identification of nonlinear aeroelastic systems

Michael McGurk*
*Aerospace Centre of Excellence, University of Strathclyde, Glasgow, UK, G1 1XJ*

Adolphus Lye†
*Singapore Nuclear Research and Safety Initiative, National University of Singapore, S(138602), Singapore*

Ludovic Renson‡
*Dynamics Group, Imperial College London, South Kensington Campus, London, SW7 2AZ, UK*

Jie Yuan§
*Computational Engineering Design Group, University of Southampton, Southampton, SO17 1BF, UK*

**The objective of this work is to propose a data-driven Bayesian inference framework to efficiently identify parameters and select models of nonlinear aeroelastic systems. The framework consists of the use of Bayesian theory together with advanced Kriging surrogate models to effectively represent the limit cycle oscillation response of nonlinear aeroelastic systems. Three types of sampling method, namely Markov Chain Monte-Carlo, Transitional Markov Chain Monte-Carlo, and the Sequential Monte-Carlo sampler, are implemented into Bayesian model updating. The framework has been demonstrated using a nonlinear wing flutter test rig. It is modelled by a two-degree-of-freedom aeroelastic system and solved by the harmonic balance methods. The experimental data of the flutter wing is obtained using control-based continuation techniques. The proposed methodology provided up to** $20\%$ **improvement in accuracy compared to conventional deterministic methods and significantly increase computational efficiency in the updating and uncertainty quantification process. Transitional Markov Chain Monte-Carlo was identified as the optimal choice of the sampling method for stochastic model identification. In selecting alternative nonlinear models, multi-modal solutions were identified that provided a closer representation of physical behaviour of the complex aeroelastic system than the single solution.**

## I. Nomenclature

*PhD Candidate, Aerospace Centre of Excellence, michael.mcgurk@strath.ac.uk
†Research Fellow, Singapore Nuclear Research and Safety Initiative, snrltsa@nus.edu.sg
‡Senior Lecturer, Dynamics Group, l.renson@imperial.ac.uk
§Assistant Professor, Computational Engineering Design Group, j.yuan@soton.ac.uk

$x$ = System degrees of freedom

$\mathbf{M}$ = Structural mass matrix

$\mathbf{D}$ = Structural damping matrix

$\mathbf{K}$ = Structural stiffness matrix

$\mathbf{A}$ = Aerodynamic inertial matrix

$\mathbf{B}$ = Aerodynamic damping matrix

$\mathbf{C}$ = Aerodynamic stiffness matrix

$V$ = Airspeed

$t$ = time

$\rho$ = Air density

$c$ = chord

$m_w$ = Mass of wing

$m_T$ = Mass of wing and support

$I_\alpha$ = Wing moment of inertia about elastic axis

$c_h$ = Heave damping coefficient

$c_\alpha$ = Pitch damping coefficient

$K_h$ = Heave linear stiffness

$K_\alpha$ = Pitch linear stiffness

$K_{\alpha 2}$ = Pitch $2^{nd}$ order nonlinear stiffness

$K_{\alpha 3}$ = Pitch $3^{rd}$ order nonlinear stiffness

$K_{\alpha 5}$ = Pitch $5^{th}$ order nonlinear stiffness

$a$,$b$,$c$ = Aerodynamic constants

## II. Introduction

A primary goal in the aerospace industry at present is to reduce $CO_2$ emissions. The use of lightweight materials and integrated electric propulsion systems is considered crucial in enhancing the efficiency and capabilities of aerospace systems. Modelling the dynamical response of lightweight aerospace structures is a challenging task because of their significant geometrical deformation, which introduces distributed nonlinearities into structures resulting in complex nonlinear dynamical behaviour [1, 2]. Furthermore, with increasing integrated systems, new interfaces can introduce localised nonlinearities, as has been observed in tiltrotor systems dynamic responses [3, 4]. The effects of these nonlinearities on dynamics and control can be very significant such as changing futter boundary in tiltrotor systems [3, 5] and shifting the aerodynamic centre of certain wings affecting control of the aircraft [6].

Due to nonlinearities in aeroelatic systems, subcritical post-flutter responses may exist [7, 8], leading to a self-sustaining oscillation occurring at velocities below the linear flutter velocity. These oscillations are referred to as Limit Cycle Oscillations (LCO) that cannot be estimated from purely linear analysis. These subcritical behaviours have been observed experimentally from high-aspect-ratio flexible wings [9, 10]. Recently, Drachinsky and Raveh [11, 12] also discovered subcritical LCO formation in experimental testing of a highly flexible wing in low-speed flutter experiments. However, the effects of nonlinearities on aeroelasticity are often neglected in computational analysis due to the added complexity and high computational cost during the design process, which greatly limits the design space of these aerospace systems. While LCO detected from nonlinear analysis can be stable, in a real system they could cause structural damage. It is therefore critical to validate mathematical models that accurately capture system nonlinear response. With reliable mathematical models the need for costly exterminates under different flow conditions would not required for certification.

This work proposes a probabilistic data-driven methodology to minimise computational burden and maximise accuracy in identifying nonlinear models to capture LCO behaviour of aeroelastic systems. Kriging models are developed with databases generated from nonlinear aeroelastic systems using harmonic balance method-based bifurcation analysis. LCO experimental data is obtained from a uniform wing test rig using control-based continuation testing methods [13]. Bayseian inference is then implemented between a Kriging surrogate model and experimental data to both estimate probabilistic parameters of the nonlinear model and rank the evidence supporting model selection. In addition, the performance of three sampling techniques are effectively compared when scholastically updating a nonlinear aeroelastic system for the first time. The implementation of a Bayesian inference in conjunction with a surrogate model to anticipate LCO behavior is a distinctive strategy in the area of aeroelasticity.

Model updating has been widely used to calibrate the parameters of mathematical or computation models based on experimental data in the last few decades. A majority of existing techniques provide deterministic estimates of parameters such as Least Squares minimisation, Sensitivity-based model updating and Levenberg-Marquardt algorithm [14–17]. Whilst direct deterministic methods are very effective for linear systems, it is subject to high computational expense for complex and high dimensional dynamical systems, and is very sensitivity to the noise in the experimental data [18]. For nonlinear aeroelastic systems, Beregi employed a classical model update approach estimate nonlinear parameters in a subcritical aerofoil test case using normal form theory. It was concluded that the accuracy of the bifurcation diagram should be improved to account for different uncertainties in the experimental data [19, 20]. Recently, researchers have acknowledged the importance of quantifying uncertainties in the nonlinear behaviour of systems, shifting the deterministic model updating approach to probabilistic ones [18, 21].

Bayesian Model Updating (BMU), first put forward in [22], is regarded as one of the most promising probabilistic nonlinear parameter estimation techniques [23–25]. A significant advantage of BMU when compared to other probabilistic model updating techniques, such as Maximum Likelihood Estimation, is its capacity to seamlessly integrate

prior knowledge [26]. With the Bayesian inference, one can assess the posterior probability density functions (PDF) by utilising the given measurement data. The posterior PDF are instrumental in providing numerical distributions for parameter estimations, along with their confidence bands [27]. The efficiency of the stochastic model updating is highly dependent on the quality of the sampling methods. Advanced iterative sampling techniques are preferred due to their ability to efficiently explore high-dimensional and correlated parameter spaces, handle non-standard posterior shapes, facilitate iterative improvement, support model comparison, and provide reliable uncertainty quantification. The most common methods are Metropolis-Hastings Markov Chain Monte Carlo (MCMC), Transitional Chain Monte Carlo (TMCMC) and the Sequential Monte Carlo sampler (SMC) [28]. Each method provides case dependent benefits, experiments are often required to select an appropriate sampling method. Comparisons between sampling methods has been carried out partially in the case of structural health monitoring[29–31]. A direct comparison does not exist for an aeroelatic test case. An advantage to TMCMC is evidence function can be calculated as a byproduct for model selection. Song et.al. utilised TMCMC in successfully selecting a nonlinear model for a wing engine structure [32].

Nonlinear System Identification (NSI) is very challenging in aeroelasticity. Firstly, the computational expense of nonlinear aeroelastic simulations is highly demanding even for low degree-of-freedom systems, especially using time domain solvers. Secondly, experimental testing of nonlinear autonomous systems is challenging due to the limitations of most linear experimental methods [13]. Thirdly, the form of nonlinear functions can be uncertain and usually lacks explicit expressions, which can make it unclear if inaccuracies between the experimental data and numerical data are down to errors in the mathematical model that is selected or errors from experimental results. When using deterministic model updating methods, it is common to face issues with parameter non-identifiability, as certain combinations of nonlinear parameters can lead to comparable results [33, 34]. Recent deterministic approaches [35–37] have shown promise in determining aeroelastic LCO but issues have been highlighted. In using universal approximates to replicate aeroelastic bifurcation diagrams, Beregi et al. [19] found cases of overiftting data. This problem is often encountered when using deterministic approaches with inherently noisy data.

Considering the computational burden in LCO simulations, little work in this area related to model updating and uncertainty quantification has been conducted [38]. The formation of LCO occurs following a hopf bifurcation that can be detected with eigenvalue analysis of underlying linear systems [39, 40]. It has been shown through both theory and experimentation that hopf bifurcations occur at the flutter points of aeroelastic systems [8, 41]. Following a hopf bifurcation, LCO characteristics are tracked through numerical continuation to produce iterative bifurcation diagrams. Recent work [42–44] has seen a focus on frequency domain techniques namely the Harmonic Balance Methods (HBM). In approximating periodic motion with Fourier series coefficients, HBM provide computationally efficient estimations in identifying the maximum response of LCO [45]. The use of HBM with continuation techniques is not essential for the proposed framework but effectively reduces computational burden of gathering training data than other numerical continuation alternatives [45].

Furthermore, the use of fast-running surrogate models can effectively be used to reduce the high computational cost of potentially thousands of nonlinear aeroelastic simulations required with BMU. Nonlinear prediction can be achieved effectively through the use of data-driven methods such as Polynomial Chaos Expansion (PCE) and neural networks [46–49]. PCE methods have been proposed specifically for UQ in aeroelastic cases in [50]. With surrogate models based on orthogonal polynomials, however the amount of training data required has shown to increase factorially with the number of design parameters [51]. Kernel-based surrogate models namely, Kriging (Gaussian Process (GP) regression) has been employed for cases with limited training data [52, 53]. Kriging models have been found to be remarkably effective in modeling complex nonlinear systems with the added benefit of requiring only minimal training data [54]. A major benefit of Kriging is the ability to seamlessly integrate new observations into the current model framework [55, 56]. Kriging surrogate models have been employed to propagate uncertainty in bifurcation diagrams of landing gear designs by Tartaruga [57] and ring damper designs by Sun et.al.[54]. Lee et.al.[58] developed a physics informed machine learnt model to improve the prediction of the bifurcation diagrams for an aerofoil test case. It showed that the deterministic estimation may lead to an overfitting problem when taking noisy data into consideration. The work also suggested that the use of nonlinear solvers, specifically those suited for periodic solutions, could enhance the training algorithms.

When identifying a system based on experimental data the two key factors to consider is the quality of the data and the amount of it. In classical wind tunnel testing, only stable LCO are detected leaving a gap in unstable sections of bifurcation diagrams. Control based continuation (CBC) first proposed by Sieber et al. [59], was introduced to perform bifurcation analysis directly in experiments. This is possible through combining Newton iterations and feedback control embedded into the continuation allowing for the detection of unstable LCO [60]. The capability of CBC has been demonstrated on several mechanical systems namely by Lee on a two-degree-of-freedom aerofoil [61]. LCO amplitude and frequency for unstable LCO was gathered presenting high-quality data for nonlinear aeroelastic system identification that will be used in this work.

This paper will first present the overall probabilistic model updating methodology for a general nonlinear aeroelastic system. It will include the process of gathering training data from HBM continuation, the development of Kriging based surrogate models, and the implementation of the Bayesian inference with MCMC, TMCMC and SMC sampling methods. The specific objectives behind the use of different MCMC-based sampling techniques is to provide a comparative study on sampling performance and its robustness towards parameter identification and model updating for a highly non-linear aeroelastic model under limited data. The three goals for the proposed methodology are (1) to provide distributions that numerically estimate nonlinear parameters; (2) to produce bifurcation plots with confidence bands; (3) to rank different forms of nonlinear models. In the following section, the mathematical model and experimentation describing a simplified nonlinear flutter test rig will be described. In the results section, nonlinear parameter estimations using the proposed methodology will be firstly presented followed by the discussion of the suitability of the nonlinear model and

the appropriate choice for the sampling method. Then, we will describe the improvement of using alternative nonlinear models through from the Bayesian model selection.

## III. Methodology

In this section, the methodology of the data-driven probabilistic modelling identification framework for a general nonlinear aeroelastic system will be presented. As shown in Figure 1, the general Methodology is divided into two parts: the development of a surrogate model describing LCO behaviour of Equation 1, and Baysian model updating with forward uncertainty quantification (UQ).The surrogate model developed in Figure 1a is created priori and left unmodified during the model updating process. With inputs gathered using Latin-Hypercube sampling (LHS), HBM continuation runs are performed following a hopf bifurcation found from the underlying linear model. Data from HBM continuation runs are used to construct surroagte models through kriging. The second stage of the methodology in Figure 1b describes the BMU process applied to the surrogate model to stochastically estimate nonlinear parameters. Each step in both the processes will be discussed as follows.

### A. Equation of motion

A general nonlinear aeroelastic system will be formulated by the following:

$$\mathbf{M}\ddot{x} + \mathbf{D}\dot{x} + \mathbf{K}x + q_{nl}f_{nl} = \mathbf{A}(\rho_{air})\ddot{x} + \mathbf{B}(\rho_{air}V)\dot{x} + \mathbf{C}(\rho_{air}V^2)x \tag{1}$$

Where $x$ denotes the system's degrees of freedom and **M**,**D** and **K** are the structural mass, damping and stiffness matrices respectively. Matrices **A B** and **C** are aerodynamic matrices which are dependent on air density and freestream velocity. All matrices are size $N \times N$ where $N$ is the number of degrees of freedom of the system. The nonlinear function $f_{nl}$ is used to represent different types of nonlinearities encountered in aeroelastic systems. The $N \times 1$ vector $q_{nl}$ is utilised to implement the nonlinear equations in the degrees of freedom they impact.

General nonlinear behaviour of a subcritical aeroelastic system is laid out in Figure 2. In the bifurcation diagram in Figure 2b a stable solution exists until a hopf bifurcation is detected at $17.8m/s$. At velocities above this point, the response of the underlying linear system to a perturbation is negatively damped. This can be determined without considering nonlinearities using standard eigenvalue analysis. Taking nonlinear effects into consideration, numerical continuation is carried out iteratively starting at the bifurcation point. Unstable LCO are identified at velocities below the bifurcation point and are tracked until a turning point. Following the turning point, stable LCO are tracked. This describes a system where two possible solutions exist between the turning point and the hopf bifurcation point, a stable damped solution and a LCO. Physically, unstable LCO represent a non-converging trajectory that exhibits instability over time. This means following nonlinear areoelastic analysis, the safe operating velocity of the system in Figure 2 is

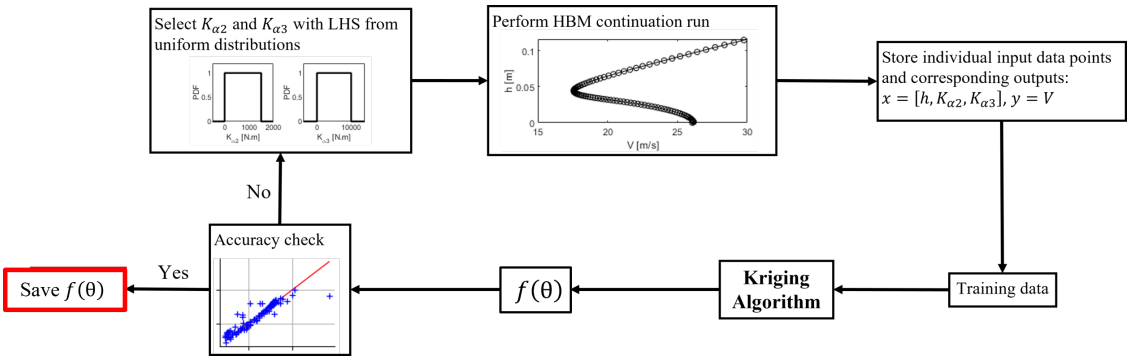


**(a) Development of Kriging surrogate models**

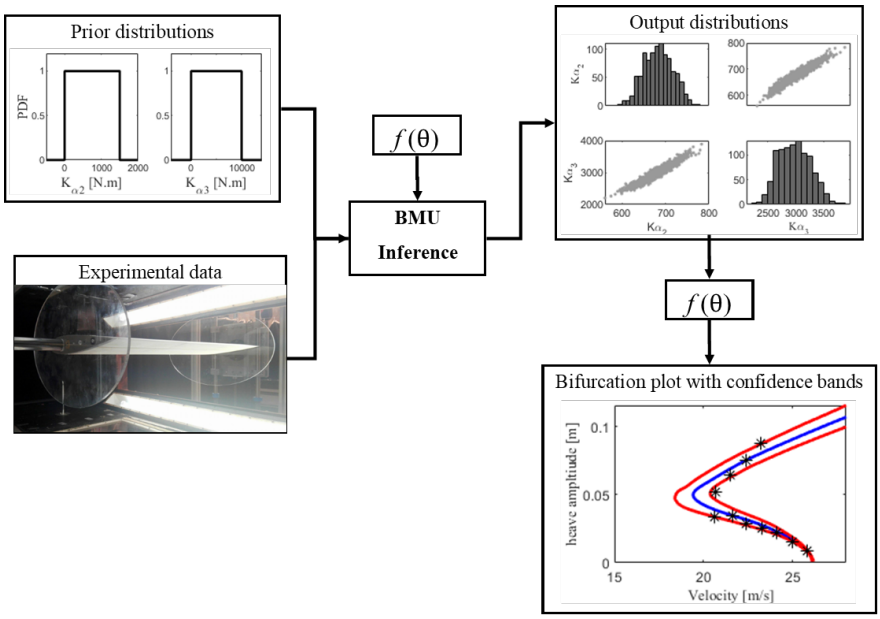


**(b) Bayesian model updating with experimental data**

**Fig. 1 The overall methodology of probabilistic identification framework for nonlinear aeroelastic systems**

shifted from $17.8 m/s$ to $13.7 m/s$ at the turning point of the bifurcation diagram.

### B. The development of surrogate models

As is observed in Fig.2b, there is a unique velocity $V$ solution for each LCO amplitude point $h$. It is possible that the Kriging surrogate model $f(h, \theta)$ can be set up as $V = f(h, \theta)$ where $\theta$ represents the vector of nonlinear parameters. In this subsection, the development of the Kriging surrogate model will be detailed. The training data for the surrogate model is first generated from deterministic simulations of nonlinear aeroelastic systems using HBM with continuation techniques. The methodology of HBM-based deterministic simulation will be briefly introduced; then the construction of Kriging surrogate models will be described.

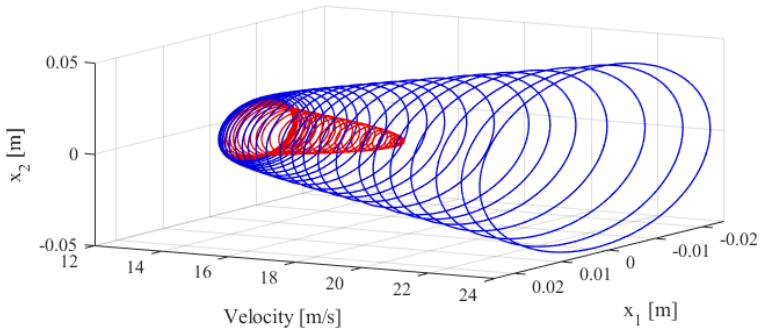


**(a) Three-dimensional subcritical bifurcation diagram**

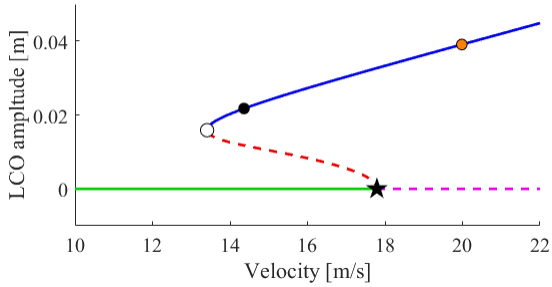


**(b) Two-dimensional subcritical bifurcation diagram (– stable solution) (- - unstable solution) (⋆ hopf bifurcation) (◯ turning point)**

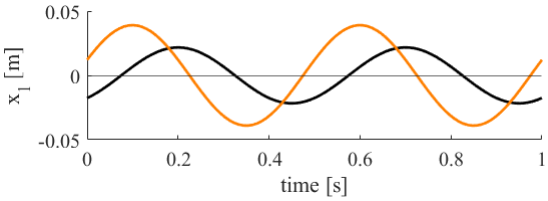


**(c) LCO time histories** $(14.5m/s\ \bullet)$ $(20m/s\ \bullet)$

**Fig. 2 Subcritical bifurcation diagram with hopf bifurcation at** $17.8m/s$ **(– stable LCO),(- - unstable LCO)**

*1. HBM based numerical continuation*

The computation of LCO behaviour is carried out through HBM coupled with continuation techniques as formulated in [45]. It is first required that the standard differential equation from Equation 1 is rearranged into first-order state Equation 2 as:

$$\dot{\mathbf{x}} = \mathbf{Q}\mathbf{x} + \mathbf{q}_n f_{nl} \tag{2}$$

Where:

$$\mathbf{x} = \begin{bmatrix} \dot{x} \\ x \end{bmatrix} \quad \mathbf{Q} = \begin{bmatrix} (\mathbf{M}-\rho\mathbf{A})^{-1}(\rho V\mathbf{B}-\mathbf{D}) & (\mathbf{M}-\rho\mathbf{A})^{-1}(\rho V^2\mathbf{C}-\mathbf{K}) \\ 0_{N\times N} & I_{N\times N} \end{bmatrix} \quad \mathbf{q_n} = \begin{bmatrix} -(\mathbf{M}-\rho\mathbf{A})^{-1}q_{nl} \\ 0_{N\times 1} \end{bmatrix}$$

Where $\mathbf{Q}$ will be referred to as the linear matrix as it fully captures the linear behaviour of the system. Flutter velocity can be found at the hopf bifurcation point considering only the linear part of the system. Equation 2 is written as the eigenvalue problem $\dot{\mathbf{x}} - \mathbf{Q}\mathbf{x} = 0$. Assuming a oscillatory response $x = x_o e^{\psi t}$ the eigenvalue problem can be written:

$$[\mathbf{Q} - \mathbf{I}\psi_i]\,\phi = 0, \tag{3}$$

where $\psi_i$ are eigenvalues in the conjugate pair

$$\psi_i = -\zeta_i \omega_i \pm i\omega_i \sqrt{1-\zeta_i} \tag{4}$$

where $i = 1...2N$ and $\omega_i$ represents damped natural frequencies and $\zeta_i$ the damping ratios. Matrix $\phi$ contains the corresponding eigenvectors. Flutter is characterised by unstable negatively damped oscillations. From this definition it can be determined that if any of the real parts of Equation 4 is positive, the system is dynamically unstable [62]. If it is assumed following a hopf bifurcation the dynamic response of the system is an LCO, the time response of $x$ and $\dot{x}$ can be represented using the Fourier series. The unknowns can be expressed by multi-harmonic response and solved in the frequency domain:

$$x(t) = X_0 + \sum_{k=1}^{l} X_{k,s} \sin k\omega t + X_{k,c} \cos k\omega t \tag{5}$$

Where $l$ represents the number of Fourier modes and $X_0$, $X_{k,s}$ and $X_{k,c}$ are Fourier coefficients. This assumed response is central to HBM, converting the system from the time domain to the frequency domain. The number of unknowns will become $(2 \times l + 1) \times N$. In addition to a set of Fourier coefficients, there is also the natural frequency of the system $\omega$ and the continuation parameter that can be any structural or aerodynamic parameters. In this case, velocity is the continuation parameter. As is common in continuation, orthogonality between a response and its differential is assumed to place an additional on the scheme [63].

Nonlinear force functions are usually modelled in time domain. Since they are not linear functions of states or explicit functions of time, it is not possible to transform directly to the frequency domain [64]. The nonlinear force response is converted to the frequency domain through the Alternating-time-frequency procedure, which is able to calculate different types of nonlinear functions even with nonsmooth nonlinearties [65]. For each iteration, the predicted values of $X_0$, $X_{k,s}$, $X_{k,c}$ and $\omega$ are used in Equations 5 to obtain the time domain response over a period. The time domain nonlinear force response $f_{nl}(t)$ is then found. A fast Fourier transform algorithm is used to estimate Fourier coefficients based on the time domain nonlinear force response. With the relationships described, the equation of motion shown in Equation 2 can be expressed into a set of algebraic residual equations, which are solved numerically using a Newton-Raphson solver [1]. The full continuation scheme is laid out in [45].

*2. Kriging algorithm*

Based on the above HBM with continuation techniques, sets of training input data $\Theta = \left[\theta^{(1)}, \theta^{(2)}, ..., \theta^{(n)}\right]$ and corresponding outputs $\mathbf{V} = \left[V^{(1)}, V^{(2)}, ..., V^{(n)}\right]$ can be gathered. In this study, LHS is used to gather the samples for the training data [66]. This choice of sampling method is standard in surrogate development for exploring diverse ranges of scenarios with minimal data. For each $\theta$ a set of $h$ and corresponding $V$ values are generated with HBM continuation scheme. Nonlinear parameters can be drawn from a distribution set by the user. Assuming no knowledge of the system,

wide uniform distributions can be typically set. This method ensures a diverse set of points along each variable. The Kriging predictor is formulated as follows:

$$f(\theta) = \mu(\theta) + \mathbf{w}^T(\theta)\mathrm{K}^{-1}(\mathbf{V} - \mu(\Theta)) \tag{6}$$

where $\mu(x)$ is the mean function that represents the expected value or trend of the response variable. It is typically assumed to be constant or can be defined based on prior knowledge or domain expertise. Covariance matrix K is an $n \times n$ matrix where $K_{ij} = Corr[x^i, x^j]$ represents the covariance or correlation between $i^{th}$ and $j^{th}$ input points. The weight factor $\mathbf{w}(x)$ is defined as

$$\mathbf{w}(x) = \mathrm{K}^{-1} Corr[x, X] \tag{7}$$

where $Corr[x, X]$ is a vector representing the correlation or covariance between input $x$ and training point $X$. In Kriging, correlation is determined based on functions in the spatial domain. Here the Matérn covariance function is used

$$Corr[x, X] = \sigma^2 \frac{2^{1-\upsilon}}{\Gamma(\upsilon)} \left( \frac{\sqrt{2\upsilon h}}{a} \right)^{\upsilon} K_{\upsilon} \left( \frac{\sqrt{2\upsilon h}}{a} \right) \tag{8}$$

where $h$ is a vector representing the separation in multiple dimensions between $x$ and $X$. Variance $\sigma$, smoothness parameter $\upsilon$ and range $a$ are determined through the optimisation process described in [67]. A Bessel function is represented by $K_{\upsilon}$ and $\Gamma(\upsilon)$ is a generalisation of the factorial function to non integer values[68].

To begin construction of the surrogate model, we firstly extract LHS samples from the uniform distributions for $\theta$ based on the initial approximations of the nonlinear parameters. Every combination undergoes a HBM continuation run. The data obtained is then segregated into individual data points that comprise velocity, amplitude, and nonlinear parameters. These points are preserved as training data and utilised to fuel the Kriging algorithm. The accuracy of the surrogate model is then validated using a set of separate data. This process is repeated until accuracy converges.

### C. The theory of Bayesian inference and sampling techniques

The Bayesian interface is implemented to estimate posterior distributions of nonlinear parameters from a prior distribution using input data and a likelihood function including experimental data. Posterior distributions of the nonlinear paramters $\theta$ are estimated with:

$$P(\theta|\mathbf{V}, f) = \frac{P(\mathbf{V}|\theta, f) . P(\theta|f)}{P(\mathbf{V}|f)} \tag{9}$$

where $f$ is the surrogate model and $\mathbf{V}$ is the vector of experimental points. The prior distribution is represented by $P(\theta|f)$, $P(\mathbf{V}|\theta, f)$ is the likelihood function, $P(\mathbf{V}|f)$ is the evidence and $P(\theta|\mathbf{V}, f)$ is the posterior distribution. The

evidence function acts as a normalising constant to ensure the posterior integrates to one. Prior distributions reflect prior knowledge of the model parameters from observations. In this work, distributions used to gather training data are selected. For a multidimensional problem such as the one discussed in this paper, distributions are combined as follows

$$P\left(\theta|f\right) = \prod_{i=1}^{n} P(\theta^{(i)}) \tag{10}$$

The likelihood function reflects the degree of agreement between obtained measurements $\mathbf{V}$ and the output of the surrogate model $f(\theta|f)$. Assuming the error between observations and the model follows a zero mean normal distribution, the likelihood function can be written as

$$P\left(\mathbf{V}|\theta, f\right) = \left(\prod_{i=1}^{n} \frac{1}{\sigma_i\sqrt{2\pi}}\right) \exp\left[-\sum_{i=1}^{n} \frac{\left(V_i - f\left(\theta^{(i)}\right)\right)^2}{2\sigma_i^2}\right] \tag{11}$$

Where $\sigma_i$ is the variance of error $\epsilon_i$ which controls the centralisation degree of the posterior distribution. Also referred to as the width parameter, $\epsilon_i$ is predetermined and case-dependent. Width parameter is selected based on the resulting acceptance rate of the samples. Acceptance rate shows the trade-off between accepting too many small steps and rejecting too many large proposal steps. Typically an acceptance rate between 0.15-0.5 ensures the algorithm's efficiency is above 80% so is aimed for [69]. Approximate Bayesian from Equation 9 (where $P(\mathbf{V}|f)$ is assumed as a constant) is evaluated by drawing samples from prior distributions until converged mean posteriors are reached. As the goal of the sampling is to converge to an unknown stationary distribution, standard methods (such as LHS used for surrogate development) are not suited. Advanced sampling techniques are therefore employed commonly for optimal efficiency[28], the three most common being MCMC, TMCMC and SMC. Each method provides unique benefits in terms of computation time, number of samples required and accuracy. The choice of sampling method is case-dependent and should be considered carefully.

The MCMC (Metropolis-Hastings method) sampler is comprised of two main features, Monte Carlo simulation and Markov chains. Introduced by Markov, a chain is initiated from $\theta_1$ and a transition to $\theta_2$ that is carried out based on a transition probability distribution function [70]. The assumption is that by allowing the chain to extend infinitely, the chain converges to a stationary distribution which corresponds to the posterior. Computation time per sample is the lowest with this method but, often a higher number of samples are required to reach a converged solution. It is common to discard a number of initial samples in what is known as the 'burn-in' to improve the quality of the results. A tuning parameter is also required with MCMC, both tuning parameter and burn-in are predefined with educated trial and error.

The TMCMC sampler is an adaptive variation of MCMC [71] and is also a specific variant of the SMC samplers (see Betz et. al [72]). A series of intermediate transitional distributions are used to gradually converge the samples towards the final posterior distribution. In addition, unlike the MCMC, it does not generate samples in a serial manner. Instead, it

generates N distinct Markov chains, each initiating from the N samples generated from the previous transition distribution and updates each chain according to its associated statistical weight. Through such approach, the TMCMC sampler is applicable towards sampling from multi-modal posteriors and have also been utilised to sample from high-dimensional posteriors (i.e., 18-dimensions) [28]. Whilst having a higher computational cost, TMCMC is automatically tuned and converges with fewer samples than MCMC commonly. Parallel computing can also be taken advantage of to improve computational efficiency.

The SMC sampler is a subset of the SMC methods that is based the Particle Filter methods typically employed for system identification purposes [73, 74]. The sampler utilises the importance sampling-resampling approach to generate samples sequentially from a dynamical posterior. Like the TMCMC sampler, the sampling procedure involves generating N distinct Markov chains, each initiating from the N samples obtained from the previous transitional distribution. The difference from the TMCMC sampler is that each Markov chain generates a new sample independently from one another (i.e. each Markov chain generates one updated sample from the starting seed sample) which allows the sampling procedure to be easily parallelised. As such, the SMC sampling approach is applicable for on-line Bayesian inference to infer either time-invariant or time-varying parameters, while the MCMC and the TMCMC samplers are only applicable for off-line Bayesian inference to infer time-invariant parameters. In addition, like the TMCMC sampler, it is also able to generate samples from multi-modal and high-dimensional posteriors. Computation time per sample is on average less than TMCMC but more than MCMC with convergence usually reached in fewer samples than MCMC. Each method will be tested in this study to evaluate which sampling method is suited to the methodology. Further detail into the Bayesian interface and each sampling method are laid out by Lye et al.[28].

Three factors are used to determine the overall quality of results: coefficient of variance, bias and $quality$ [72]. Coefficient of variance ($COV = \frac{std}{\mu}$) is used to determine the confidence of a prediction where $std$ is the standard deviation and $\mu$ is the mean of the prediction from BMU. Bias is calculated with

$$bias = \frac{|\mu - e|}{e} \tag{12}$$

Where $e$ is the corresponding true experimental point to $\mu$. This gives a measure of accuracy only considering the mean prediction and not confidence bands. A completely accurate prediction would give a $bias$ of zero. Taking confidence of prediction into account, $bias$ and $COV$ are used to calculate $quality$.

$$quaility = \sqrt{bias^2 + COV^2} \tag{13}$$

Combining both confidence and accuracy, $quality$ is the main factor used to determine overall accuracy. An ideal prediction would have a $quality$ of zero. These factors will be calculated by comparing bifurcation plots using BMU

predictions of nonlinear parameters to experimental data for both configurations.

Forward uncertainty quantification is performed by running the output distributions through $f(\theta)$. This produces a bifurcation plot with 95% confidence bands. In theory, the mean solution should give a close approximation of the true bifurcation plot. It could also be argued, if all input experimental data fall within the confidence bands a reasonable approximation of true uncertainty in the predicted parameters has been captured. If data points lie outside of the confidence bands, it may suggest the mathematical model does not truly represent dynamic behaviour or there has been errors obtaining the experimental data.

### D. TMCMC based class selection

One of the key advantages of the Bayesian interface is in model selection. With the evidence term, the validity of models can be ranked. The evidence term is not required in the cases of MCMC but can be numerically estimated[75]. With regards to TMCMC sampling method, the evidence for specific model $f$, $P(\mathbf{V}|f))$ is a byproduct required for estimation of the statistical weight function $w$ used to describe the importance of each sample[76]. The model selection with TMCMC sampling is formulated in [76]. The TMCMC algorithm draws samples from a series of intermediate distributions, generated iteratively with the capability of converging to complex multi-modal posterior distributions. These PDFs are defined as:

$$P_j \propto P(\theta|f) \cdot P(\mathbf{V}|f,\theta)^{\beta_j} \qquad j = 0, ..., m \tag{14}$$

Where $j$ is the stage number. Tempering parameter $\beta$ evolves from $\beta_0 = 0$ to $\beta_m = 1$ to ensure a smooth transition between the prior and posterior distribution so $P_0 = P(\theta|f)$ to $P_m = P(\theta|f,\mathbf{V})$. The weight of each sample is determined as:

$$w\left(\theta_{j,k}\right) = \frac{P(\theta|f) \cdot P(\mathbf{V}|f,\theta)^{\beta_{j+1}}}{P(\theta|f) \cdot P(\mathbf{V}|f,\theta)^{\beta_j}} = P(\mathbf{V}|f,\theta)^{\beta_{j+1}-\beta_j} \qquad k = 1, ..., N_j \tag{15}$$

Where $N$ is the number of samples. Next, compute

$$S_j = \frac{\sum_{k=1}^{N_j} w(\theta_{j,k})}{N_j} \tag{16}$$

This process is repeated for each stage. At the end of the algorithm, the evidence of the model can be computed as

$$P(\mathbf{V}|f) = \prod_{j=0}^{m-1} S_j \tag{17}$$

It is common to evaluate $\log(P(\mathbf{V}|f))$ for ease of computation, mainly to avoid numerical problems (e.g. arithmetic underflow) associated with the calculation of the full likelihood function [28]. The less negative $\log(P(\mathbf{V}|f))$ the more evidence there is to suggest the specific model fits the provided data.

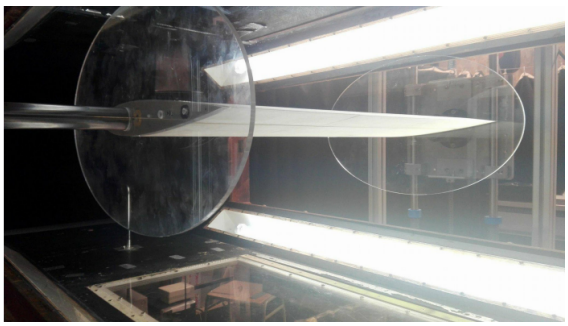

(a) Experimental configuration [61]

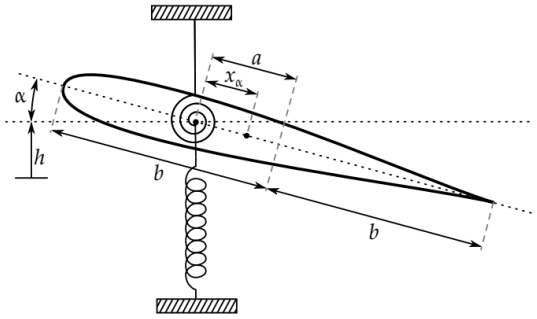


(b) 2 DOF Freebody diagram

**Fig. 3 Nonlinear flutter test rig**

## IV. Model description

In this section the experimental flutter rig and the mathematical model that will be used to study the proposed probabilistic identification framework are described.

### A. Experimental configuration and data collection

Figure 3a shows the experimental flutter rig comprised of a NACA-0015 wing profile rigidly attached to a stainless steel shaft. The aerofoil is supported by rotational bearings on each end allowing for rotation and a bearing system allowing vertical displacement. The spring in the heavy degree of freedom behaves in a linear manner. In the bearings, leaf springs are introduced to create a nonlinear hardening effect in pitch motion. This mimics nonlinear effects at interfaces that are encountered in a real aircraft. Detailed description of the set-up is found in [37]. An Omron ZX1-LD300 laser displacement sensor is used to measure heave displacement and a RLS AksIM 18 bit absolute magnetic encoder captures pitch motion. Wind speed was recorded directly from the wind tunnel control system. Both stable and unstable LCO are captured through control-based-continuation. The raw data was fed into a fast Fourier transform algorithm to minimise noise. This process was carried out for two experimental configuration with different spring constants. LCO amplitude and corresponding velocity for each configuration is displayed in Figure 4 with design rig parameters for both in 1. Data was collected using control-based continuation, providing access to both stable and unstable responses of the system (see [61] for more explanations about CBC and its exploitation in this context). Based on two sets of experimental data, $K_{\alpha 2}$ and $K_{\alpha 3}$ were determined by implementing the deterministic approach normal form theory in [61]. The estimated values are shown in Table 1 and will be used as the initial input points.

### B. Mathematical model

The flutter rig is modelled as the two-degree-of-freedom system shown in Figure 3b coupled with an unsteady aerodynamic model described by Abdelkef et al. [77]. For the nonlinear flutter rig considered $x = [h, \alpha, w]$ where $h$ is heave, pitch is $\alpha$ and $w$ is the aerodynamic state. The structural matrices as shown in Equation1 are configuration as:

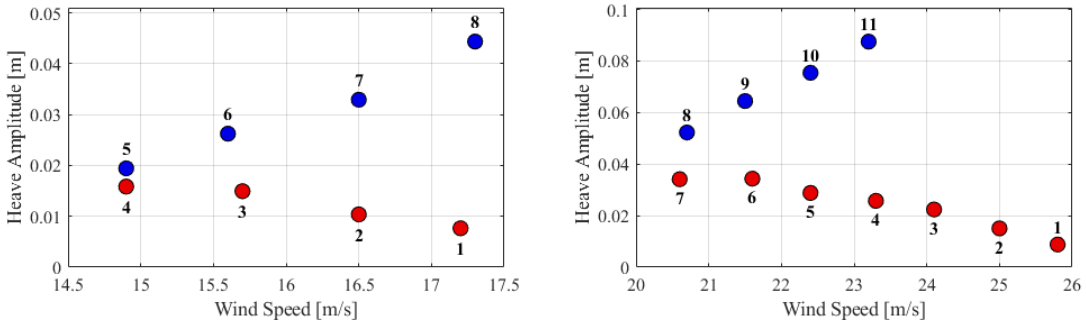


**(a) configuration 1** **(b) configuration 2**

**Fig. 4 Labelled experimental data (• stable LCO) (• unstable LCO)**

$$\mathbf{M} = \begin{bmatrix} m_T & m_w x_\alpha b & 0 \\ m_w x_\alpha b & I_\alpha & 0 \\ 0 & 0 & 1 \end{bmatrix}; \quad \mathbf{D} = \begin{bmatrix} c_h & 0 & 0 \\ 0 & c_\alpha & 0 \\ -1/b & a - 1/2 & 0 \end{bmatrix}; \quad \mathbf{K} = \begin{bmatrix} K_h & 0 & 0 \\ 0 & K_\alpha & 0 \\ 0 & 0 & 0 \end{bmatrix} \tag{18}$$

The unsteady aerodynamic matrices are described as follows:

$$\mathbf{A} = \begin{bmatrix} -\pi b^2 & a\pi b^3 & 0 \\ a\pi b^3 & -\pi\left(1/8 + a^2\right) b^4 & \\ 0 & 0 & 1 \end{bmatrix}$$

$$\mathbf{B} = \begin{bmatrix} -\pi b & -\left(1 + (1/2 - a)\right) \pi b^2/\rho & -2\pi V b \left(c_1 c_2 + c_3 c_4\right)/\rho \\ \pi \left(a + 1/2\right) b^2/V & -\left(1/4 - a^2\right) \pi b^3 & 2\pi b^2 V \left(a + 1/2\right) \left(c_1 c_2 + c_3 c_4\right) \\ 0 & 0 & -\left(c_2 + c_4\right)/\rho b \end{bmatrix} \tag{19}$$

$$\mathbf{C} = \begin{bmatrix} 0 & -\pi b & -2\pi V c_2 c_4 \left(c_1 + c_3\right)/\rho \\ 0 & \pi b^2 \left(1/2 + a\right) & 2\pi b \left(a + 1/2\right) c_2 c_4 \left(c_1 + c_3\right) \\ 0 & 1/\rho V b & c_2 c_4/\rho b^2 \end{bmatrix}$$

Where $\mathbf{A}, \mathbf{B}, \mathbf{C}$ are the corresponding martix in Equation 1. To model the nonlinear part of the system it is initially assumed spring stiffness is approximated by quadratic and cubic terms in pitch degree of freedom (which is typically

**Table 1 Measured parameters and estimated parameters including initial estimates for nonlinear parameters**

| Measured Parameters | Value | Estimated Parameters | Initial estimated value |
|---|---|---|---|
| $c(m)$ | 0.15 | $K_h(N/m)$ | 3529.4 (configuration 1), 3318.3 (configuration 2) |
| $a$ | −0.5 | $K_\alpha(N/rad)$ | 54.11 (configuration 1), 65.6 (configuration 2) |
| $\rho(kg/m^3)$ | 1.204 | $K_{\alpha 2}(N/rad^2)$ | 751.6 (configuration 1), 774.7 (configuration 2) |
| $m_w(kg)$ | 5.3 | $K_{\alpha 3}(N/rad^3)$ | 5006.7 (configuration 1), 3490.7 (configuration 2) |
| $m_T$ | 16.9 | $c_\alpha(kgm^2/s^2)$ | 0.5628 (configuration 1), 1.0338 (configuration 2) |
| $x_\alpha$ | 0.24 | | |
| $I_\alpha$ | 0.1724 | | |
| $c_h(kg/s)$ | 14.5756 | | |

used to represent geometrical nonlinearities [78]):

$$f_{nl} = K_{\alpha 2}\alpha^2 + K_{\alpha 3}\alpha^3; \quad q_{nl} = \begin{bmatrix} 0 \\ 1 \\ 0 \end{bmatrix} \tag{20}$$

Nonlinear parameters $K_{\alpha 2}$ and $K_{\alpha 3}$ are treated as unknowns. The methodology described in this paper will work to estimate the nonlinear parameters. Other known parameter values are listed in Table 1.

## V. Results: comparison of sampling methods

In this section, the described probabilistic identification methodology proposed in the section 2 is applied to the two configurations of the above nonlinear flutter test rig. It is assumed that original nonlinear function is in a form shown in Equation 20 as in previous work [19, 37, 58, 61]. Considering the reference data in [58], we assume that $K_{\alpha 2}$ is in the range of $0 - 1500N/rad^2$ while $K_{\alpha 3}$ is in the range of $0 - 10000N/rad^3$. For each setup, three sampling methods, namely MCMC, TMCMC and SMC sampling methods, are applied and compared in terms of the quality factors of the model identification. These results are also compared to the initial estimates obtained form normal from theory [58] and listed in Table 1.

Figure 5 shows mean accuracy of Kriging surrogate models with respect to the amount of training continuation runs carried out. Here, mean accuracy is estimated based on the difference between predictions from the Kriging model and a separate set of comparison data from continuation runs. Accuracy converges with 400 bifurcation diagrams in training data at 99.8%. The same amount of training data is again required for the second configuration. Figure 6 compares the amplitude of LCO obtained from HBM simulation and the Kriging surrogate model. The highlighted area reflects the degree of uncertainty from the predictions using the Kriging model within 95% confidence bands. Small discrepancies are observed at turning points as sharpness of the curve is increased which was not improved

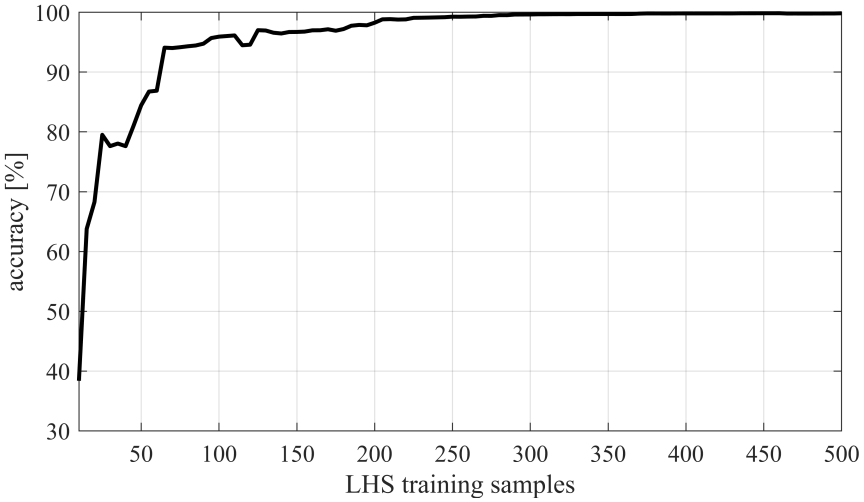


**Fig. 5 Accuracy of surrogate model with respect to sample size for configuration 1**

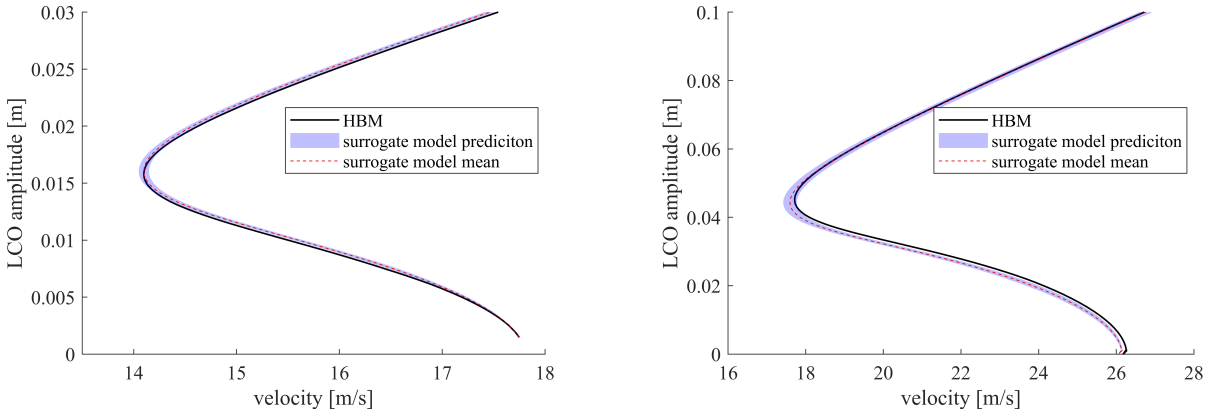


**(a) configuration 1** **(b) configuration 2**

**Fig. 6 Surrogate comparison**

with increased sampling. The largest overshoot of the turning point observed was 2% (shown in Figure 6b which was considered within a reasonable margin of error for this study. Uncertainty in model predictions close to estimated values for nonlinear parameters proved to be less an 1% on average. It was therefore assumed that the mean predictions of the surrogate model were accurate in the subsequent Bayesian parameter estimation process, and the uncertainty associated with the surrogate model was not incorporated into the parameter estimation. With mean predictions, it is observed that the Kriging model is capable of accurately capturing the response of LCO.

### A. Configuration 1

Bayesian inference framework is firstly applied to the first configuration with the experimental data shown in Figure 4a. Tuning parameters presented in Table 2 are used to ensure an acceptance rate between 0.15-0.5 for each sampling

**Table 2 Tuning parameters**

| Prior distribution bounds | Width parameter | Burn-in | Covariance matrix |
|---|---|---|---|
| $K_{\alpha_2}$: 0 - 1500 | MCMC: 0.6 | 200 | [ 1000 0 ] |
| $K_{\alpha_3}$: 0 - $1e^4$ | TMCMC: 1 | 0 | [ 0 7000 ] |
| | SMC: 0.1 | 0 | |

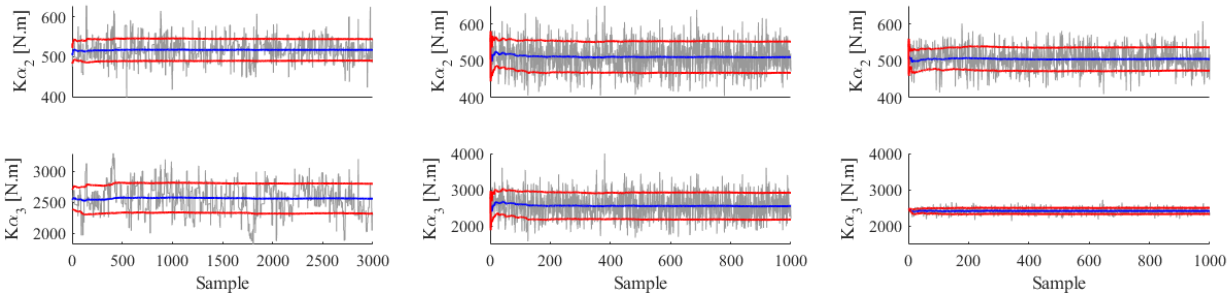


**(a) MCMC (acceptance rate = 0.267)** **(b) TMCMC (acceptance rate = 0.44)** **(c) SMC (acceptance rate = 0.32)**

**Fig. 7 configuration 1 trace plots (– mean),(– mean ± $std$)**

method. Prior distributions are uniform between the stated bounds as low prior knowledge of the parameters is assumed. Figure 7 shows the convergence of nonlinear parameters with three sampling methods. The convergence is defined as when the mean and standard deviation of the posterior distribution becomes constant with further sampling. It shows that TMCMC and SMC can converge within 300 samples while MCMC required 2736 samples with additional 200 burn-in samples before the convergence. It is worth noting that SMC converges in the fewest samples with only 153 mainly due to the benefit of using importance sampling. With TMCMC and SMC less samples are required for model updating than in construction of the surrogate model. This seems to suggest there is no need to construct a surrogate model. However, with the goal of using the estimated parameter distributions to quantity the impact of uncertainty on bifurcation diagrams, the surrogate models are again implemented, significantly reducing computation time.

Figure 8 shows the Probability Density Functions (PDFs) and scatter plots using three different sampling methods. It can be observed that each sampling method produces a PDF that resembles a normal distribution. The mean and $COV$ of estimated nonlinear parameters are presented in Table 3. The estimated mean of the nonlinear parameter between these three sampling methods is within 15%. It is worth noting that the estimation of the mean is around 45% different from the initial estimates shown in Table 1. For both parameters, TMCMC provides the smallest confidence interval in parameter prediction. It is also found that the two nonlinear parameters are linearly correlated from MCMC and TMCMC, which however is not observed with the SMC sampling method as no samples are rejected during the sampling process.

Figure 9 shows the distributed bifurcation diagrams using the estimated nonlinear parameters from the Bayesian model updating. It is observed both TMCMC and SMC results capture all experimental data points within their 95%

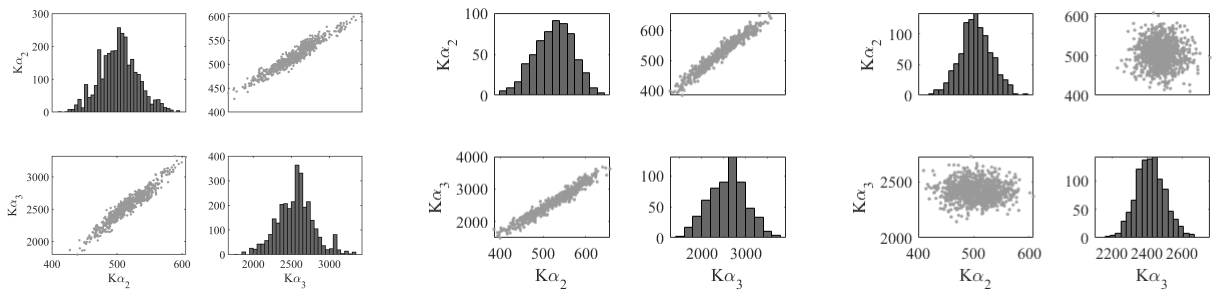

(a) MCMC (b) TMCMC (c) SMC

**Fig. 8 configuration 1 PDF and scatter plots**

**Table 3 set up 1 parameter estimation**

| | MCMC | | TMCMC | | SMC | |
|---|---|---|---|---|---|---|
| | $K_{\alpha 2}$ | $K_{\alpha 3}$ | $K_{\alpha 2}$ | $K_{\alpha 3}$ | $K_{\alpha 2}$ | $K_{\alpha 3}$ |
| mean | 517.20 | 2555.8 | 524.50 | 2595.9 | 505.08 | 2420.6 |
| COV [%] | 5.52 | 9.44 | 9.72 | 16.20 | 6.29 | 3.47 |
| Convergence (samples) | 2736 | | 215 | | 153 | |

uncertainty bands. In the case of MCMC, the confidence interval is much narrower than that using TMCMC and SMC. There are two data points in the upper portion of the diagram falling outside uncertainty bands. It can be also found that the lowest band of the turning point in MCMC and TMCMC spans to $14m/s$ while this point is at $12.20m/s$ for SMC. If we are to assume the mathematical model is correct it indicates that SMC appears to overestimate the uncertainty of LCO.

Figure 10 shows a comparison of mean lines from three sampling methods, the initial estimate and experimental data. A clear improvement can be observed with each of the sampling methods compared to the one using the initial estimates. The estimation of the LCO amplitude in each method closely follows the experimental data at the low amplitude points but diverges after the turning point. The mean lines from each method closely follows each other, only overshooting

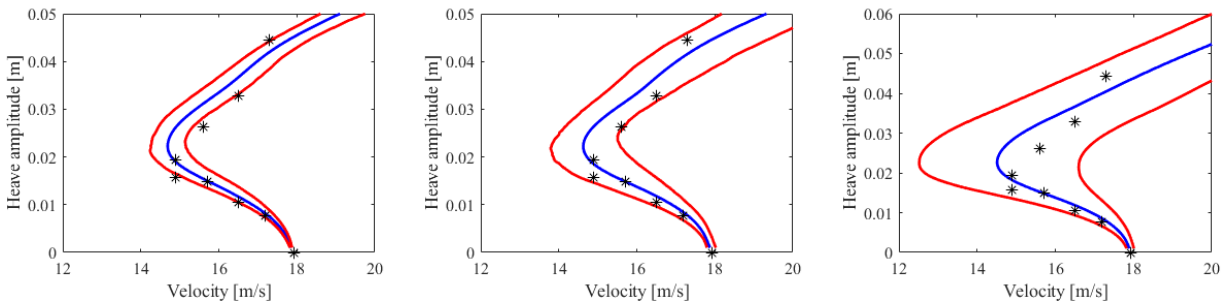


(a) MCMC (b) TMCMC (c) SMC

**Fig. 9 configuration 1 bifurcation plots (* experimental points)(– mean plot), (– 95% confidence bounds)**

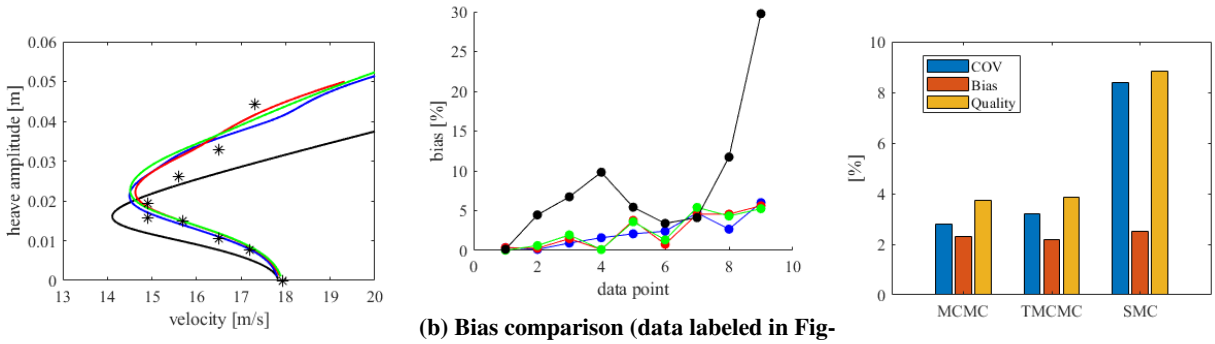


**(a) Mean comparison** **(b) Bias comparison (data labeled in Figure 4a)** **(c) Quality comparison**

**Fig. 10 configuration 1 comparison (* experimental points),(– initial estimate),(– MCMC),(– TMCMC),(– SMC)**

**Table 4 set up 2 parameter estimation**

| | **MCMC** | | **TMCMC** | | **SMC** | |
|---|---|---|---|---|---|---|
| | $K_{\alpha 2}$ | $K_{\alpha 3}$ | $K_{\alpha 2}$ | $K_{\alpha 3}$ | $K_{\alpha 2}$ | $K_{\alpha 3}$ |
| mean | 700.03 | 3122.4 | 678.32 | 2982.6 | 697.20 | 3040.8 |
| COV [%] | 4.00 | 7.66 | 5.26 | 9.41 | 3.76 | 3.32 |
| Convergence (samples) | 2531 | | 207 | | 160 | |

the turning point by $0.3m/s$. Figure 10b shows the bias of these four methods in relation to experimental data. Each sampling method is more accurate than the initial estimate for all data points apart from the point 7. The accuracy for all sampling methods remains above 94% without a sharp drop off in accuracy. Figure 10c shows the quality of the prediction between these three sampling method. It shows MCMC and TMCMC provide the best overall estimation of physical behaviour in terms of confidence and accuracy. The bias of all methods are within 3%. However, the relatively large $COV$ in SMC predictions leads to a higher $quality$ than the other two sampling methods.

### B. Configuration 2

Using the same method for configuration 1, a surrogate model for configuration 2 is constructed with 386 continuation runs required for training data. The tuning parameters presented in Table 2 were implemented for model updating in set up 2. Figure 11 shows the convergence of each sampling method where the similar pattern is observed as the first set up. The SMC sampling method remains as the fastest converging one with only 200 samples. Figure 12 shows scatter plots and PDFs produced. In this case, each of the sampling methods provide a shape similar to a normal distribution for both parameters. A strong correlation between the parameters is again observed with results from MCMC and TMCMC but not SMC. The mean and $COV$ from the estimations are shown in Table 4. It can be seen that the mean results from the Bayesian model updating are closer to the initial estimates shown in Table 1. The most confident predictions are again achieved with SMC achieving the lowest average COV.

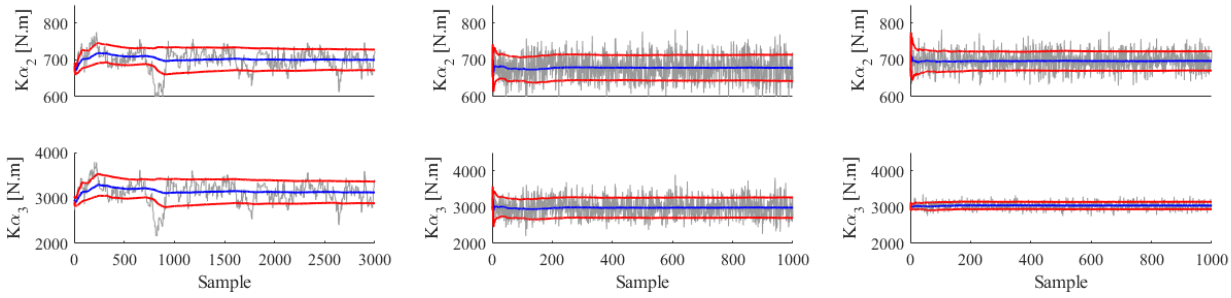


**(a) MCMC (acceptance rate = 0.30)** **(b) TMCMC (acceptance rate = 0.43)** **(c) SMC (acceptance rate = 0.36)**

**Fig. 11 Set up 2 trace plots (– mean),(– mean ± $std$)**

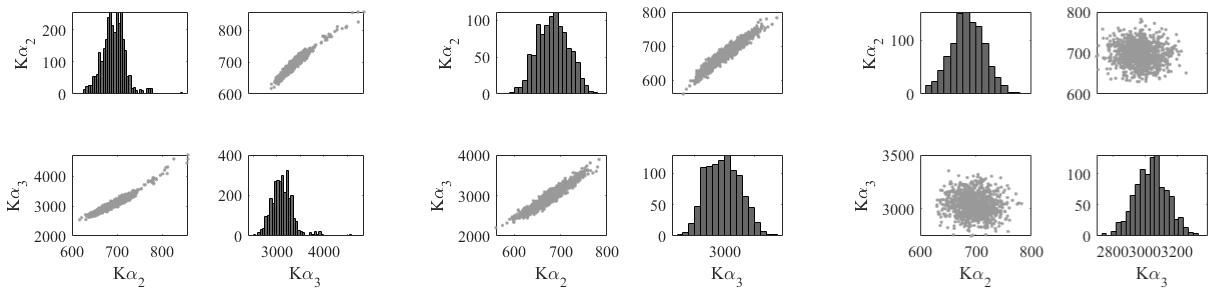


**(a) MCMC** **(b) TMCMC** **(c) SMC**

**Fig. 12 Set up 2 PDF and scatter plots**

Figure 13 shows the bifurcation plot with confidence interval using the estimated posterior distribution of estimations. Similar results are observed to the first set up, with SMC capturing all data points with a wide confidence bands while MCMC and TMCMC only captures LCO behaviour at low amplitude before the turning point. Again, the MCMC does not capture two data points after the turning point and TMCMC misses only one point. The lower band of SMC significantly overshoots the turning point. As shown in Figure 14a, the mean line from each sampling method is compared to the response generated with the initial estimate. In this case, it is less obvious which prediction is more accurate. At lower amplitudes, the initial estimate matches the behaviour but after the turning point, the accuracy is

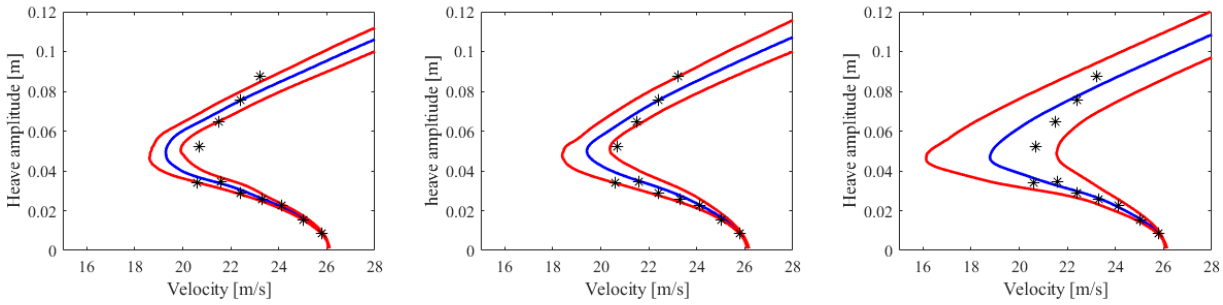


**(a) MCMC** **(b) TMCMC** **(c) SMC**

**Fig. 13 Set up 2 bifurcation plots (* experimental points)(– mean plot), (– 95% confidence bounds)**

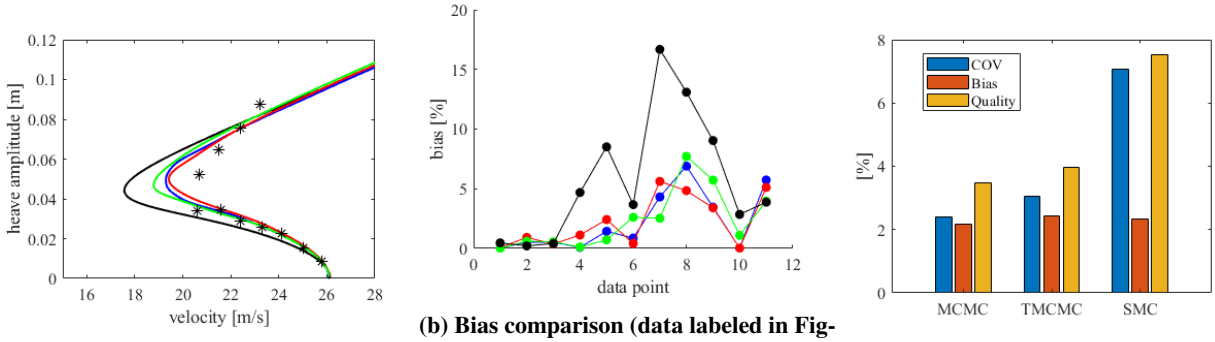


**(a) Mean comparison**

**(b) Bias comparison (data labeled in Figure 4b)**

**(c) Quality comparison**

**Fig. 14 Set up 2 comparison (* experimental points),(– initial estimate),(– MCMC),(– TMCMC),(– SMC)**

lost. The mean lines from BMU predictions offer a slight improvement over the initial estimate. The initial estimate overshoots the turning point the most. Figure 14b shows a comparison of bias of all the predictions compared to the experimental points. It is observed, the initial estimate is most accurate until the turning point. For the stable LCO, predictions from MCMC and TMCMC provide the most accurate predictions. Figure 14c confirms similar conclusions to the Figure 10c where MCMC and TMCMC show best overall quality.

### C. Conclusions of sampling method comparison

Considering both configurations several conclusions are reached. The experimental data is captured well using BMU leading to better estimations than deterministic results. In the second configuration, the predicted results for both BMU and the initial estimate appear in better agreement than in the first configuration. This could mean the mathematical model holds better for the second set-up or there were fewer errors in gathering the experimental results. Another reason could be the increased number of experimental data points used in the estimation. Considering overall mean accuracy, each sampling method outperformed the initial estimate, particularly at higher amplitudes. Each sampling method can be argued for depending on whether the user prioritises the accuracy of the mean prediction or a combination of accuracy and confidence. If confidence and mean prediction is valued MCMC provides the best estimation. In contrast, if capturing all physical behaviour is preferred, TMCMC and SMC may be chosen despite being the overshoot of the turning point especially in the case of SMC. Parameter estimations have the lowest $COV$ with SMC sampling but provide the widest confidence bands in their bifurcation plots. This is likely due to SMC not rejecting samples and not observing correlations between parameters. Both TMCMC and SMC converge with less samples than training input runs are required, however taking forward UQ into consideration up to 60% less HBM continuation runs are required.

Taking all factors into account, TMCMC provides the best overall compromise in terms of convergence and accuracy for both configurations. In configuration 1 the bifurcation plot produced captures all data points without significantly overshooting the turning point and over 90% of data for configuration 2. The estimations from TMCMC and SMC in configuration 1 capture all physical behaviour within their confidence bands, which suggests the parameter distributions

accurately estimate the true uncertainty of the parameters and the mathematical model hold, particularly in the case of TMCMC. For these reasons, it may be argued the estimated distributions of nonlinear parameters can effectively represent physical behaviour. Alternatively, there is less agreement between all predicted values and experimental data after the turning point. There are two possible reasons: the model only holds for low amplitude results or there was a measurement error in gathering higher amplitude points. For the first case, the form of the model needs to be modified to capture higher amplitude behaviour. Since the errors become larger as amplitude increases, it is more likely the aerodynamic model does not hold for higher amplitude in this scenario, but further investigation is required.

Based on the results from both setups a clear pattern has emerged in that lower amplitude data points are well captured but accuracy is lost in upper sections in both BMU and initial estimates. There may be two reasons the experimental data may not match the results: (1) there was a significant amount of noise or errors in gathering the data; (2) the mathematical model particularly the nonlinear function may not fully capture the true physical behaviour of the system. In an effort to further improve the accuracy of mathematical models to capture the experimental data, alternative nonlinear models are suggested and ranked in the next section.

## VI. Results: Nonlinear model selection

Previously it was assumed both $K_{\alpha 2}$ and $K_{\alpha 3}$ were positive. Prior distributions and LHS for surrogate models for nonlinear parameters could not draw samples from negative design space. In this section, prior distributions that include negative design space are considered. The aim is to improve agreement with results from model updating and experimental data by altering the characteristic of the nonlinear function. Figure 15 shows examination of the whole design space. The turning point of all bifurcation plots involving cubic hardening are below $12m/s$ for configuration 1, overshooting what would be expected from the experimental results by over 25%. The same behaviour was observed in configuration 2. For this reason cubic hardening design space is not considered. As seen in [38], the third and fifth-order non-linearity is also considered in sub-critical aerofoil systems. With the same criteria as in Figure 15, this nonlinearity's only feasible design space is with third-order softening and fifth-order hardening spring.

$$f_{nl} = \pm K_{\alpha 3}\alpha^3 \pm K_{\alpha 5}\alpha^5 \tag{21}$$

Table 5 shows the three possible nonlinear models to approximate the experimental LCO data. The suitability of the models will be ranked by both the average $quality$ of the bifurcation results and the evidence function $\log(P(D|M))$ from BMU with TMCMC sampling.

The Kriging surrogate models for each nonlinear function are first developed through the same methodology presented in the Section 2. The TMCMC sampling method is selected for BMU since it has proved the most effective method using the original nonlinearity in the previous section. It can also produce the evidence function as a by-product

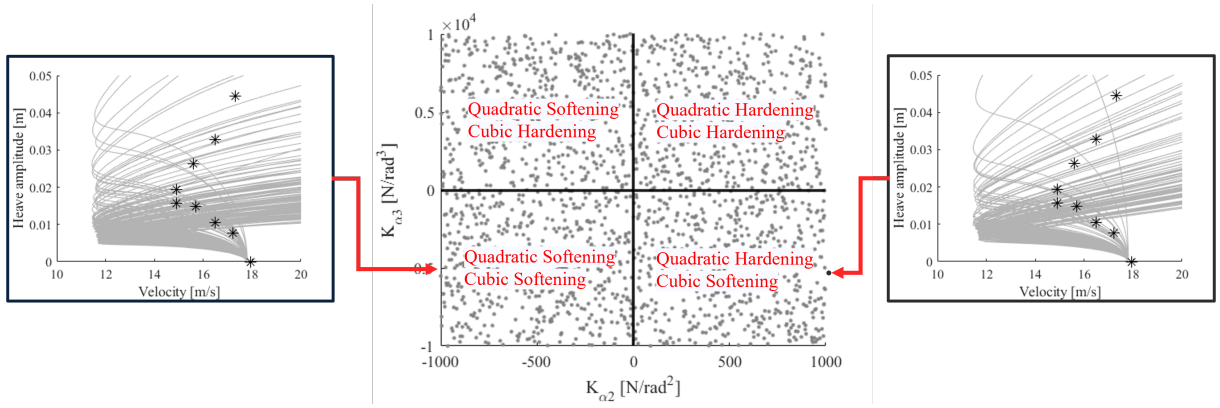


**Fig. 15 Full model selection design space. Each point on the scatter plot represents a full bifurcation diagram**

**Table 5 Parameter estimations for model selection**

| | Model | Parameters[Units] | Mean | $COV$ [%] |
|---|---|---|---|---|
| **1** | $K_{\alpha 2} + K_{\alpha 3}$ | $K_{\alpha 2}$,$K_{\alpha 3}$ | 524.50,2595.9 (configuration 1) | 9.72,16.20 (configuration 1) |
| | | $[N/rad^2]$,$[N/rad^3]$ | 678.32,2982.6 (configuration 2) | 5.26,9.41 (configuration 2) |
| **2** | $-K_{\alpha 2} + K_{\alpha 3}$ | $K_{\alpha 2}$,$K_{\alpha 3}$ | $-383.78$,1442.1 (configuration 1) | 12.20, 22.17 (configuration 1) |
| | | $[N/rad^2]$,$[N/rad^3]$ | $-530.99$,1754.2 (configuration 2) | 4.20,7.84 (configuration 2) |
| **3** | $-K_{\alpha 3} + K_{\alpha 5}$ | $K_{\alpha 3}$,$K_{\alpha 5}$ | $-1822.5$,$1.136e^5$ (configuration 1) | 22.01,31.14 (configuration 1) |
| | | $[N/rad^3]$,$[N/rad^5]$ | $-2343.5$,$1.061e^5$ (configuration 2) | 19.27,21.55 (configuration 2) |

for the model selection. It was found the evaluation of $\log(P(D|M))$ required additional samples to converge over mean and standard deviation values. Table 6 shows that $\log(P(D|M))$ converges at 10000 samples. For each model with both configurations, 10000 samples are taken to ensure evidence function converged. Tables 5 and 7 display the estimated parameters for each model and the evidence function compared to the average $quaility$ of predictions.

As shown in the Table 6, model 3 provided the highest variation in predicted parameters for both configurations. For configuration 1, model 1 has the highest confidence in estimations and model 2 has the highest for configuration 2 having the lowest average $COV$ respectively.

Table 7 shows the computed evidence of each model for the two configurations. It can be observed that, for configuration 1, the evidence function indicates model 2 is the best choice whereas model 1 has the lowest $quaility$ factor. Figure 16 shows that nonlinear model 1 and 2 capture all data within confidence bands. The bifurcation plots produced from all models show plots that closely resemble each other. The model 3 fails to capture one data point from the confidence bands after the turning point. Figure 16 shows a closer examination of the PDFs of nonlinear parameters.

**Table 6 Convergence of evidence function for configuration 1, model 1 with TMCMC sampling**

| Samples | 100 | 500 | 1000 | 2500 | 5000 | 7500 | 10000 | 125000 |
|---|---|---|---|---|---|---|---|---|
| $\log(P(D\|M))$ | -7.83 | -7.94 | -7.72 | -7.35 | -7.44 | -7.46 | -7.45 | -7.45 |

**Table 7 Evidence function for configuration 1 and 2 from 10000 TMCMC samples**

| | | configuration 1 | | configuration 2 | |
|---|---|---|---|---|---|
| | $f_{nl}$ | $\log(P(D\|M))$ | $quality$ [%] | $\log(P(D\|M))$ | $quality$ [%] |
| **1** | $K_{\alpha 2} + K_{\alpha 3}$ | −7.45 | 5.24 | −8.86 | 5.21 |
| **2** | $-K_{\alpha 2} + K_{\alpha 3}$ | −5.30 | 5.61 | −9.74 | 5.01 |
| **3** | $-K_{\alpha 3} + K_{\alpha 5}$ | −5.68 | 8.74 | −8.77 | 4.78 |

It is very clear that multi-modal distributions are produced for the model 2 and 3, suggesting the existence of two possible solutions. The mode with the highest probability density is referred to as peak 1 while peak 2 refers to the lower probability density peak. The model 3 has a single modal solution for $K_{\alpha 3}$ but a multi-modal solution for $K_{\alpha 5}$. Figures 18a and 18b show the response of LCO using the nonlinear parameters estimated from each peak. For model 2, it can be observed peak 1 fails to capture the highest amplitude point but has a closer overall fit to the experimental data. The response using the nonlinear parameters from the Peak 2 reaches the highest amplitude point but stays away from the remaining data at amplitudes above the turning point. In model 3, peak 1 captures lower amplitude data and the highest amplitude point. Peak 2 captures data close to the turning point while failing to reach the highest amplitude points.

Considering just average quality, results suggest the model 1 is the optimal choice for configuration 1. This is in line with the bifurcation diagram capturing all experimental points within confidence bands. Based on the TMCMC class selection, both models 2 and 3 are recommended above model 1. However, the solutions to these models are multi-modal as discussed. Since there are two suggested solutions, it is not valid to just consider the mean and $COV$ of the posterior distribution estimations. This suggests considering a combination of the two different nonlinear functions at different LCO amplitudes might provide a better model than the single solution provided by model 1. Quality measurement assumes there is a single estimated solution whereas evidence function can account for multimodal results. This is why quality and evidence functions recommend alternative solutions in both configurations.

In configuration 2 both evidence function and $quaility$ suggest model 3 is the optimal choice. The examination of posterior distributions in Figure 14 shows that models 1 and 2 converge to a unique solution while model 3 produces a multi-modal PDF with two possible solutions. Figure 18c show the amplitude of LCO with these two possible solutions. It shows peak 1 captures lower amplitude data while peak 2 the higher amplitude points. As was the case with configuration 1, TMCMC model selection favours a combination between these two possible solutions which outperforms a single solution from the original model. Overall this could mean that none of the models are perfect, particularly with higher amplitude points an updated model is required.

## VII. Conclusion

In this paper, a probabilistic identification methodology for estimating parameters in a nonlinear aeroelastic system is presented. An advanced kriging algorithm is used to develop accurate data-driven surrogate models for LCO behaviour.

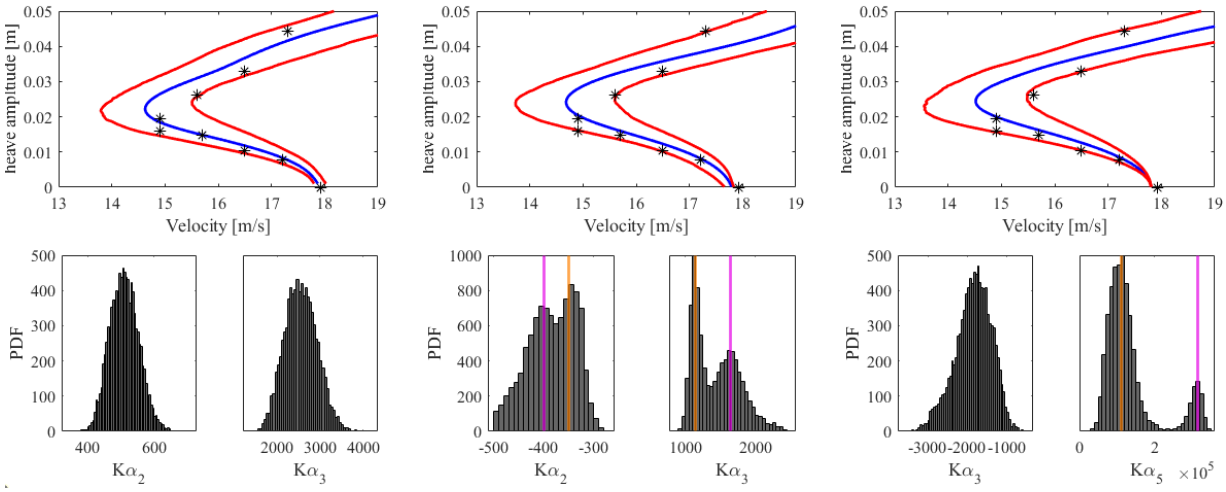


**(a) Model 1** **(b) Model 2** **(c) Model 3**

**Fig. 16 Bifurcation diagrams and PDF for configuration 1 [for multi-modal PDF (– peak 1),(– peak 2)]**

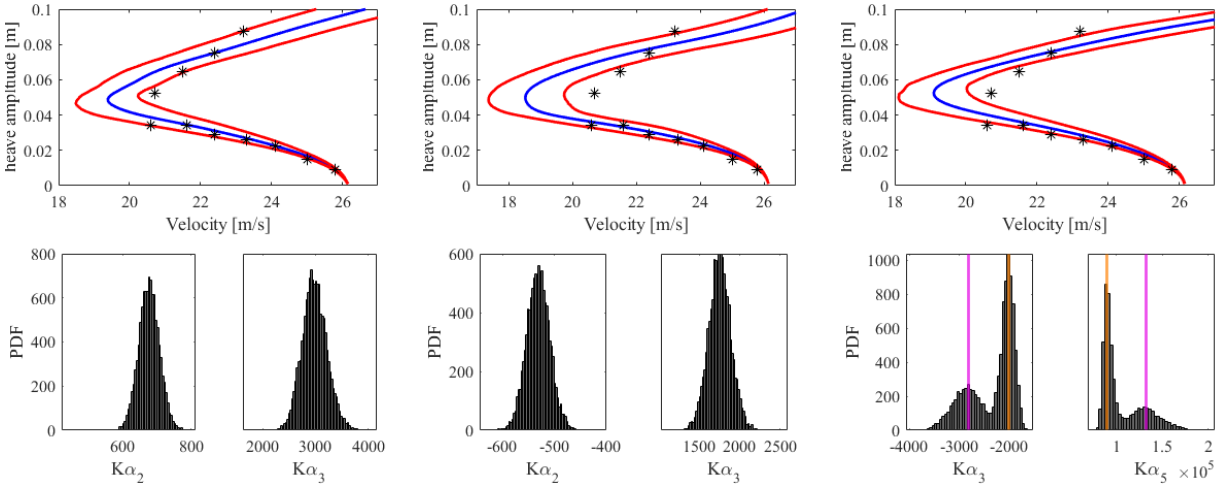


**(a) Model 1** **(b) Model 2** **(c) Model 3**

**Fig. 17 Bifurcation diagrams and PDF for configuration 1 [for multi-modal PDF (– peak 1),(– peak 2)]**

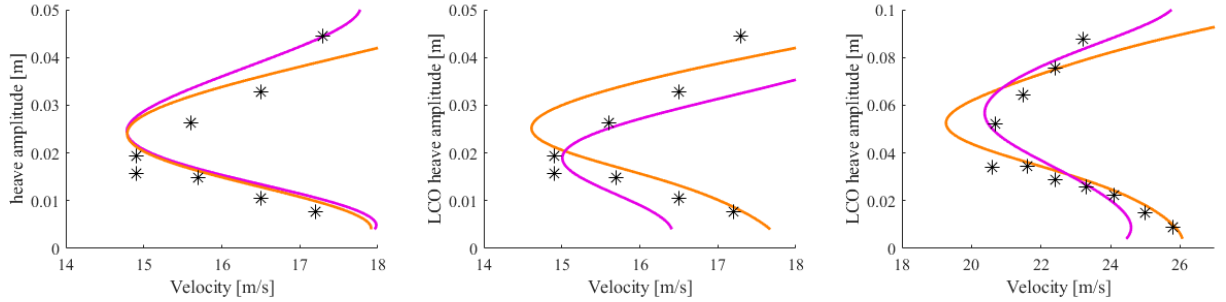


**(a) configuration 1, model 2** **(b) configuration 1, model 3** **(c) configuration 2, model 3**

**Fig. 18 Multi-modal mean bifurcation diagrams (– peak 1),(– peak 2)**

The surrogate models are employed with BMU to identify the nonlinear parameters and functions. The performance of three advanced sampling methods are compared. Experimental data from the nonlinear flutter rig with two separate configurations was employed with the goal of estimating a nonlinear model to fit the data.

Probabilistic bifurcation diagrams produced with BMU successfully captured the experimental data was within the computed confidence bands at low amplitude points. This proved a significant improvement from the initial deterministic approach for each configuration. With higher amplitude points portions of the data were not captured within confidence bands but made an improvement over the initial estimate. Results from BMU for each sampling method had variations due to the different sampling philosophies associated with each respective approach. In the first configuration, TMCMC and SMC could capture all data points within confidence bands while SMC overshoots the estimation of the turning point by a large margin. The correlation between nonlinear parameters was also observed in MCMC and TMCMC results. Only SMC could capture all physical behaviour while overshooting the turning point in the second configuration. The estimations from the TMCMC is able to capture over 90% of the physical behaviour leading to an average mean accuracy of 98%. Considering the accuracy and convergence, it was determined TMCMC produced the highest quality estimations, capturing all experimental points with much higher convergence than MCMC. All predictions with estimations from BMU were up to 20% more accurate than that from the initial estimate. Accuracy in prediction of physical behaviour following the turning point dropped. From 5% to 22% of data points are omitted from confidence bands following the turning point. This suggests the mathematical model does not hold for higher amplitudes of LCO, and a more sophisticated aerodynamic model might be needed. Considering computational efficiency, for purely estimating mean nonlinear parameters more HBM continuation runs are required with TMCMC and SMC with the data-driven approach. In carrying out forward UQ however, the proposed methodology can cut the amount of costly continuation runs by up to 60%.

Two categories of nonlinear models were implemented and evaluated through TMCMC class selection. For the first configuration, the TMCMC process suggested selecting model 2, which includes quadratic softening and cubic hardening. As for the second configuration, model 3 equipped with third-order softening and fifth-order hardening was deemed the most suitable option. After analyzing the quality factor of results obtained from the bifurcation diagrams along with the confidence bands for both scenarios, it can be concluded that model 1 is the most suitable option. An examination of posterior PDFs of nonlinear parameters showed the presence of multi-modal solutions in both configurations. Taking a single mean and standard deviation estimation from either of two estimated solutions did not capture the complete set of data. Upon examining both solutions, it was noted that each solution is capable of capturing a portion of the bifurcation diagram either for lower or upper amplitude data. TMCMC class selection suggests there is no unique solution to represent the nonlinear functions to capture all the physic across a wide range of amplitude, particularly for higher amplitude points. A further improvement of the mathematical model for the nonlinear aeroelastic model is required. This could either be achieved with an alternative nonlinear function or implementing nonlinearities in

different degrees of freedom. Another area of improvement could be in optimising the amount of training data required for constructing the surrogate models, potentially with a multi-level approach. This would integrate the Kriging model with the model updating process.

## Acknowledgements

M. McGurk acknowledge the support from the EPSRC Doctoral Training Partnership (DTP) studentship for his PhD study at the University of Strathclyde. J.Yuan also acknowledges the funding support of the Royal Academy of Engineering/Leverhulme Trust Research Fellowship (LTRF2223-19-150).

## Data acknowledgement

The authors acknowledge the experimental work by Kyoung Hyun Lee. Experimental data is available at https://github.com/Kyounghyunlee/

## References


[1] Dimitriadis, G., *Introduction to nonlinear aeroelasticity*, John Wiley & Sons, 2017.

[2] Ghaffari, R., and Sauer, R. A., "Modal analysis of graphene-based structures for large deformations, contact and material nonlinearities," *Journal of Sound and Vibration*, Vol. 423, 2018, pp. 161–179. https://doi.org/https://doi.org/10.1016/j.jsv.2018.02.051.

[3] Quintana, A. G., Saunders, B. E., Vasconcellos, R., and Abdelkefi, A., "Nonlinear characterization of the piecewise structural effects on whirl flutter of a rotor-nacelle system," *AIAA SCITECH 2022 Forum*, 2022, p. 2269. https://doi.org/https://doi.org/10.2514/6.2022-2269.

[4] Mair, C., Rezgui, D., and Titurus, B., "Nonlinear stability analysis of whirl flutter in a tiltrotor rotor-nacelle system," *43rd European Rotorcraft Forum 2017*, 2017.

[5] Quintana, A., Vasconcellos, R., Throneberry, G., and Abdelkefi, A., "Nonlinear analysis and bifurcation characteristics of whirl flutter in unmanned aerial systems," *Drones*, Vol. 5, No. 4, 2021, p. 122. https://doi.org/https://doi.org/10.3390/drones5040122.

[6] Phillips, W., Alley, N., and Niewoehner, R., "Effects of nonlinearities on subsonic aerodynamic center," *Journal of aircraft*, Vol. 45, No. 4, 2008, pp. 1244–1255. https://doi.org/https://doi.org/10.2514/1.34241.

[7] Shukla, H., and Patil, M. J., "Nonlinear state feedback control design to eliminate subcritical limit cycle oscillations in aeroelastic systems," *Nonlinear Dynamics*, Vol. 88, 2017, pp. 1599–1614. https://doi.org/https://doi.org/10.1007/s11071-017-3332-5.

[8] Guckenheimer, J., and Holmes, P., *Nonlinear oscillations, dynamical systems, and bifurcations of vector fields*, Vol. 42, Springer Science & Business Media, 2013.

[9] Tang, D., and Dowell, E. H., "Experimental and theoretical study on aeroelastic response of high-aspect-ratio wings," *AIAA journal*, Vol. 39, No. 8, 2001, pp. 1430–1441. https://doi.org/https://doi.org/10.2514/2.1484.

[10] Patil, M. J., Hodges, D. H., and Cesnik, C. E., "Limit-cycle oscillations in high-aspect-ratio wings," *Journal of fluids and structures*, Vol. 15, No. 1, 2001, pp. 107–132. https://doi.org/https://doi.org/10.1006/jfls.2000.0329.

[11] Avin, O., Raveh, D. E., Drachinsky, A., Ben-Shmuel, Y., and Tur, M., "An experimental benchmark of a very flexiblewing," *AIAA Scitech 2021 Forum*, 2021, p. 1709. https://doi.org/https://doi.org/10.2514/6.2021-1709.

[12] Drachinsky, A., Avin, O., Raveh, D. E., Ben-Shmuel, Y., and Tur, M., "Flutter tests of the Pazy wing," *AIAA Journal*, Vol. 60, No. 9, 2022, pp. 5414–5421. https://doi.org/https://doi.org/10.2514/1.J061717.

[13] Barton, D. A., Mann, B. P., and Burrow, S. G., "Control-based continuation for investigating nonlinear experiments," *Journal of Vibration and Control*, Vol. 18, No. 4, 2012, pp. 509–520. https://doi.org/https://doi.org/10.1177/1077546310384004.

[14] Kaba, A., Metin, E. Y., and Turan, O., "Thrust modelling of a target drone engine with nonlinear least–squares estimation based on series expansions," *Aircraft Engineering and Aerospace Technology*, , No. ahead-of-print, 2022. https://doi.org/https://doi.org/10.1108/AEAT-08-2021-0236.

[15] Eiselt, H., Sandblom, C.-L., et al., *Nonlinear optimization*, Springer, 2019.

[16] Friswell, M., and Mottershead, J. E., *Finite element model updating in structural dynamics*, Vol. 38, Springer Science & Business Media, 1995.

[17] Patelli, E., Govers, Y., Broggi, M., Gomes, H. M., Link, M., and Mottershead, J. E., "Sensitivity or Bayesian model updating: a comparison of techniques using the DLR AIRMOD test data," *Archive of Applied Mechanics*, Vol. 87, 2017, pp. 905–925. https://doi.org/https://doi.org/10.1007/s00419-017-1233-1.

[18] Bi, S., Beer, M., Cogan, S., and Mottershead, J., "Stochastic Model Updating with Uncertainty Quantification: An Overview and Tutorial," *Mechanical Systems and Signal Processing*, Vol. 204, 2023, p. 110784. https://doi.org/https://doi.org/10.1016/j.ymssp.2023.110784.

[19] Beregi, S., Barton, D. A., Rezgui, D., and Neild, S., "Using scientific machine learning for experimental bifurcation analysis of dynamic systems," *Mechanical Systems and Signal Processing*, Vol. 184, 2023, p. 109649. https://doi.org/https://doi.org/10.1016/j.ymssp.2022.109649.

[20] Stolovitch, L., "Progress in normal form theory," *Nonlinearity*, Vol. 22, No. 7, 2009, p. R77. https://doi.org/https://doi.org/10.1088/0951-7715/22/7/R01.

[21] Yuan, J., Denimal, E., Bi, S., Feng, J., Hu, Q., and Cicirello, A., "Special Section on Uncertainty Quantification and Management in Nonlinear Dynamical Systems in Aerospace and Mechanical Engineering," *ASCE-ASME J Risk and Uncert in Engrg Sys Part B Mech Engrg*, Vol. 9, No. 4, 2023. https://doi.org/https://doi.org/10.1115/1.4063301.

[22] Beck, J. L., and Katafygiotis, L. S., "Updating models and their uncertainties. I: Bayesian statistical framework," *Journal of Engineering Mechanics*, Vol. 124, No. 4, 1998, pp. 455–461.

[23] Namdeo, V., and Manohar, C., "Nonlinear structural dynamical system identification using adaptive particle filters," *Journal of Sound and Vibration*, Vol. 306, No. 3-5, 2007, pp. 524–563. https://doi.org/https://doi.org/10.1016/j.jsv.2007.05.040.

[24] Green, P. L., and Worden, K., "Bayesian and Markov chain Monte Carlo methods for identifying nonlinear systems in the presence of uncertainty," *Philosophical Transactions of the Royal Society A: Mathematical, Physical and Engineering Sciences*, Vol. 373, No. 2051, 2015, p. 20140405. https://doi.org/https://doi.org/10.1098/rsta.2014.0405.

[25] Ebrahimian, H., Astroza, R., and Conte, J. P., "Extended Kalman filter for material parameter estimation in nonlinear structural finite element models using direct differentiation method," *Earthquake Engineering & Structural Dynamics*, Vol. 44, No. 10, 2015, pp. 1495–1522. https://doi.org/https://doi.org/10.1002/eqe.2532.

[26] Yin, M., Iannelli, A., and Smith, R. S., "Maximum likelihood estimation in data-driven modeling and control," *IEEE Transactions on Automatic Control*, 2021. https://doi.org/https://doi.org/10.1109/TAC.2021.3137788.

[27] Noël, J.-P., and Kerschen, G., "Nonlinear system identification in structural dynamics: 10 more years of progress," *Mechanical Systems and Signal Processing*, Vol. 83, 2017, pp. 2–35. https://doi.org/https://doi.org/10.1016/j.ymssp.2016.07.020.

[28] Lye, A., Cicirello, A., and Patelli, E., "Sampling methods for solving Bayesian model updating problems: A tutorial," *Mechanical Systems and Signal Processing*, Vol. 159, 2021, p. 107760. https://doi.org/https://doi.org/10.1016/j.ymssp.2021.107760.

[29] Rocchetta, R., Broggi, M., Huchet, Q., and Patelli, E., "On-line Bayesian model updating for structural health monitoring," *Mechanical Systems and Signal Processing*, Vol. 103, 2018, pp. 174–195. https://doi.org/https://doi.org/10.1016/j.ymssp.2017.10.015.

[30] Zhang, Y., and Yang, W., "A comparative study of the stochastic simulation methods applied in structural health monitoring," *Engineering Computations*, Vol. 31, No. 7, 2014, pp. 1484–1513. https://doi.org/https://doi.org/10.1108/EC-07-2013-0185.

[31] Fang, C., Liu, H.-J., Lam, H.-F., Adeagbo, M. O., and Peng, H.-Y., "Practical model updating of the Ting Kau Bridge through the MCMC-based Bayesian algorithm utilizing measured modal parameters," *Engineering Structures*, Vol. 254, 2022, p. 113839. https://doi.org/https://doi.org/10.1016/j.engstruct.2022.113839.

[32] Song, M., Renson, L., Moaveni, B., and Kerschen, G., "Bayesian model updating and class selection of a wing-engine structure with nonlinear connections using nonlinear normal modes," *Mechanical Systems and Signal Processing*, Vol. 165, 2022, p. 108337. https://doi.org/https://doi.org/10.1016/j.ymssp.2021.108337.

[33] Walter, E., and Pronzato, L., "On the identifiability and distinguishability of nonlinear parametric models," *Mathematics and computers in simulation*, Vol. 42, No. 2-3, 1996, pp. 125–134. https://doi.org/https://doi.org/10.1016/0378-4754(95)00123-9.

[34] Quaranta, G., Lacarbonara, W., and Masri, S. F., "A review on computational intelligence for identification of nonlinear dynamical systems," *Nonlinear Dynamics*, Vol. 99, No. 2, 2020, pp. 1709–1761. https://doi.org/https://doi.org/10.1007/s11071-019-05430-7.

[35] Gui, G., Liu, F., Sun, J., Yang, J., Zhou, Z., and Zhao, D., "Flight delay prediction based on aviation big data and machine learning," *IEEE Transactions on Vehicular Technology*, Vol. 69, No. 1, 2019, pp. 140–150. https://doi.org/https://doi.org/10.1109/TVT.2019.2954094.

[36] Gábor, A., and Banga, J. R., "Robust and efficient parameter estimation in dynamic models of biological systems," *BMC systems biology*, Vol. 9, No. 1, 2015, pp. 1–25. https://doi.org/https://doi.org/10.1186/s12918-015-0219-2.

[37] Lee, K., Barton, D., and Renson, L., "Mathematical Model Identification of Self-Excited Systems Using Experimental Bifurcation Analysis Data," *Nonlinear Structures & Systems, Volume 1: Proceedings of the 40th IMAC, A Conference and Exposition on Structural Dynamics 2022*, Springer, 2022, pp. 61–63. https://doi.org/https://doi.org/10.1007/978-3-031-04086-3_9.

[38] Riso, C., Cesnik, C. E., and Epureanu, B. I., "Bifurcation-Diagram-Free Postflutter Response Constraint for Design Optimization," *AIAA Journal*, 2023, pp. 1–18. https://doi.org/https://doi.org/10.2514/1.J062012.

[39] Seydel, R., *Practical bifurcation and stability analysis*, Vol. 5, Springer Science & Business Media, 2009.

[40] Lanza, V., Bonnin, M., and Gilli, M., "On the application of the describing function technique to the bifurcation analysis of nonlinear systems," *IEEE Transactions on Circuits and Systems II: Express Briefs*, Vol. 54, No. 4, 2007, pp. 343–347. https://doi.org/https://doi.org/10.1109/TCSII.2006.890406.

[41] Tartaruga, I., Barton, D., Rezgui, D., and Neild, S., "Experimental bifurcation analysis of a wing profile," *Proc. of International Forum on Aeroelasticity and Structural Dynamics*, 2019, pp. 9–13.

[42] Gudmundson, P., "On The Accuracy Of The Harmonic-Balance Method Concerning Vibrations Of Beams With Nonlinear Supports." *Archive of applied mechanics (1991)*, Vol. 59, No. 5, 1989, pp. 333–344. https://doi.org/https://doi.org/10.1007/BF00534063.

[43] Razzak, M. A., "A simple harmonic balance method for solving strongly nonlinear oscillators," *Journal of the Association of Arab Universities for Basic and Applied Sciences*, Vol. 21, 2016, pp. 68–76. https://doi.org/https://doi.org/10.1016/j.jaubas.2015.10.002.

[44] Detroux, T., Renson, L., Masset, L., and Kerschen, G., "The harmonic balance method for bifurcation analysis of large-scale nonlinear mechanical systems," *Computer Methods in Applied Mechanics and Engineering*, Vol. 296, 2015, pp. 18–38. https://doi.org/https://doi.org/10.1016/j.cma.2015.07.017.

[45] McGurk, M., and Yuan, J., "Computation of limit cycle oscillations and their stabilities in nonlinear aeroelastic systems using harmonic balance methods," *Proceedings of the International Forum on Aeroelasticity and Structural Dynamics*, Madrid, 2022.

[46] Zhou, Y., and Lu, Z., "Active polynomial chaos expansion for reliability-based design optimization," *AIAA Journal*, Vol. 57, No. 12, 2019, pp. 5431–5446. https://doi.org/https://doi.org/10.2514/1.J058020.

[47] Agrawal, S., Gobiha, D., and Sinha, N., "Nonlinear parameter estimation of airship using modular neural network," *The Aeronautical Journal*, Vol. 124, No. 1273, 2020, pp. 409–428. https://doi.org/https://doi.org/10.1017/aer.2019.125.

[48] Verma, H., and Peyada, N., "Estimation of aerodynamic parameters near stall using maximum likelihood and extreme learning machine-based methods," *The Aeronautical Journal*, Vol. 125, No. 1285, 2021, pp. 489–509. https://doi.org/https://doi.org/10.1017/aer.2020.95.

[49] Yuan, J., Fantetti, A., Denimal, E., Bhatnagar, S., Pesaresi, L., Schwingshackl, C., and Salles, L., "Propagation of friction parameter uncertainties in the nonlinear dynamic response of turbine blades with underplatform dampers," *Mechanical Systems and Signal Processing*, Vol. 156, 2021, p. 107673. https://doi.org/https://doi.org/10.1016/j.ymssp.2021.107673.

[50] Hosder, S., Walters, R., and Balch, M., "Efficient uncertainty quantification applied to the aeroelastic analysis of a transonic wing," *46th AIAA Aerospace Sciences Meeting and Exhibit*, 2008, p. 729. https://doi.org/https://doi.org/10.2514/6.2008-729.

[51] Weinmeister, J., Gao, X., and Roy, S., "Analysis of a polynomial chaos-Kriging metamodel for uncertainty quantification in aerodynamics," *AIAA Journal*, Vol. 57, No. 6, 2019, pp. 2280–2296. https://doi.org/https://doi.org/10.2514/1.J057527.

[52] Palar, P. S., Zakaria, K., Zuhal, L. R., Shimoyama, K., and Liem, R. P., "Gaussian processes and support vector regression for uncertainty quantification in aerodynamics," *AIAA Scitech 2021 Forum*, 2021, p. 0181. https://doi.org/https://doi.org/10.2514/6.2021-0181.

[53] Yildiz, S., Cakmak, E., Kara, E., and Nikbay, M., "Uncertainty quantification of aeroelastic systems using active learning gaussian process," *Proceedings of the International Conference on Multidisciplinary Design Optimization of Aerospace Systems (AEROBEST 2021), Virtual Event, Online*, 2021, pp. 21–23.

[54] Sun, Y., Denimal, E., Yuan, J., and Salles, L., "Geometric design of friction ring dampers in blisks using nonlinear modal analysis and Kriging surrogate model," *Structural and Multidisciplinary Optimization*, Vol. 65, No. 3, 2022, p. 98. https://doi.org/https://doi.org/10.1007/s00158-021-03093-w.

[55] Lee, D., Kang, Y.-E., Kim, D.-H., and Yee, K., "Aeroelastic Design and Comprehensive Analysis of Composite Rotor Blades Through Cluster-Based Kriging," *AIAA Journal*, Vol. 60, No. 10, 2022, pp. 5984–6004. https://doi.org/https://doi.org/10.2514/1.J061820.

[56] Peng, X., Kou, J., and Zhang, W., "Multi-fidelity Nonlinear Unsteady Aerodynamic Modeling and Uncertainty Estimation Based on Hierarchical Kriging," *Applied Mathematical Modelling*, 2023. https://doi.org/https://doi.org/10.1016/j.apm.2023.05.031.

[57] Tartaruga, I., Cooper, J., Lowenberg, M., Sartor, P., and Lemmens, Y., "Uncertainty and sensitivity analysis of bifurcation loci characterizing nonlinear landing-gear dynamics," *Journal of Aircraft*, Vol. 55, No. 1, 2018, pp. 162–172. https://doi.org/https://doi.org/10.2514/1.C034252.

[58] Lee, K., Barton, D., and Renson, L., "Modelling of physical systems with a hopf bifurcation using mechanistic models and machine learning," *Mechanical Systems and Signal Processing*, Vol. 191, 2023, p. 110173. https://doi.org/https://doi.org/10.1016/j.ymssp.2023.110173.

[59] Sieber, J., and Krauskopf, B., "Control based bifurcation analysis for experiments," *Nonlinear Dynamics*, Vol. 51, No. 3, 2008, pp. 365–377. https://doi.org/https://doi.org/10.1007/s11071-007-9217-2.

[60] Sieber, J., Krauskopf, B., Wagg, D., Neild, S., and Gonzalez-Buelga, A., "Control-based continuation of unstable periodic orbits," 2011. https://doi.org/https://doi.org/10.1115/1.4002101.

[61] Lee, K., Barton, D., and Renson, L., "Model identification of a fluttering aerofoil using control-based continuation and normal form analysis," *Proceedings of the International Conference on Noise and Vibration Engineering, ISMA*, 2020, pp. 261–268.

[62] Wright, J. R., and Cooper, J. E., *Introduction to aircraft aeroelasticity and loads*, Vol. 20, John Wiley & Sons, 2008.

[63] Govaerts, W., *Numerical bifurcation analysis for ODEs*, Journal of Computational and Applied Mathematics, 2000. 125(1–2), 57–68.

[64] Cameron, T., and Griffin, J. H., "An alternating frequency/time domain method for calculating the steady-state response of nonlinear dynamic systems," 1989. https://doi.org/https://doi.org/10.1115/1.3176036.

[65] Yuan, J., Sun, Y., Schwingshackl, C., and Salles, L., "Computation of damped nonlinear normal modes for large scale nonlinear systems in a self-adaptive modal subspace," *Mechanical Systems and Signal Processing*, Vol. 162, 2022, p. 108082. https://doi.org/https://doi.org/10.1016/j.ymssp.2021.108082.

[66] Scarth, C., Cooper, J. E., Weaver, P. M., and Silva, G. H., "Uncertainty quantification of aeroelastic stability of composite plate wings using lamination parameters," *Composite Structures*, Vol. 116, 2014, pp. 84–93. https://doi.org/https://doi.org/10.1016/j.compstruct.2014.05.007.

[67] Airbus-EDF-IMACS-ONERA-Phimeca, "OpenTURNS," , 2022. URL https://openturns.github.io/www/.

[68] Minasny, B., and McBratney, A. B., "Spatial prediction of soil properties using EBLUP with the Matérn covariance function," *Geoderma*, Vol. 140, No. 4, 2007, pp. 324–336. https://doi.org/https://doi.org/10.1016/j.geoderma.2007.04.028.

[69] Roberts, G. O., and Rosenthal, J. S., "Optimal scaling for various Metropolis-Hastings algorithms," *Statistical science*, Vol. 16, No. 4, 2001, pp. 351–367. https://doi.org/https://doi.org/10.1214/ss/1015346320.

[70] Serfozo, R., *Basics of applied stochastic processes*, Springer Science & Business Media, 2009.

[71] Beck, J. L., and Au, S.-K., "Bayesian updating of structural models and reliability using Markov chain Monte Carlo simulation," *Journal of engineering mechanics*, Vol. 128, No. 4, 2002, pp. 380–391. https://doi.org/https://doi.org/10.1061/(ASCE)0733-9399(2002)128:4(380).

[72] Betz, W., Papaioannou, I., and Straub, D., "Transitional Markov chain Monte Carlo: observations and improvements," *Journal of Engineering Mechanics*, Vol. 142, No. 5, 2016, p. 04016016. https://doi.org/https://doi.org/10.1061/(ASCE)EM.1943-7889.0001066.

[73] Ristic, B., Arulampalam, S., and Gordon, N., *Beyond the Kalman filter: Particle filters for tracking applications*, Artech house, 2003.

[74] Green, P. L., Devlin, L., Moore, R. E., Jackson, R. J., Li, J., and Maskell, S., "Increasing the efficiency of Sequential Monte Carlo samplers through the use of approximately optimal L-kernels," *Mechanical Systems and Signal Processing*, Vol. 162, 2022, p. 108028. https://doi.org/https://doi.org/10.1016/j.ymssp.2021.108028.

[75] Chib, S., and Jeliazkov, I., "Marginal likelihood from the Metropolis–Hastings output," *Journal of the American statistical association*, Vol. 96, No. 453, 2001, pp. 270–281. https://doi.org/https://doi.org/10.1198/016214501750332848.

[76] Ching, J., and Chen, Y.-C., "Transitional Markov chain Monte Carlo method for Bayesian model updating, model class selection, and model averaging," *Journal of engineering mechanics*, Vol. 133, No. 7, 2007, pp. 816–832. https://doi.org/https://doi.org/10.1061/(ASCE)0733-9399(2007)133:7(816).

[77] Abdelkefi, A., Vasconcellos, R., Nayfeh, A. H., and Hajj, M. R., "An analytical and experimental investigation into limit-cycle oscillations of an aeroelastic system," *Nonlinear Dynamics*, Vol. 71, No. 1, 2013, pp. 159–173. https://doi.org/https://doi.org/10.1007/s11071-012-0648-z.

[78] Lee, K. H., “Bifurcation-based Ordinary Differential Equation Model Identification,” (PhD thesis), 2023, pp. 36–39.